Research Paper

Investigation of hybrid sensible-latent packed bed thermal energy storage system

Asem Alemam [a,*] , Saman Nimali Gunasekara [b], Justin NingWei Chiu [b] , Klarissa Niedermeier [c], Imran Afgan [a]

[a] Department of Mechanical and Nuclear Engineering, College of Engineering and Physical Sciences, Khalifa University, Abu Dhabi 127788, United Arab Emirates
[b] Department of Energy Technology, KTH Royal Institute of Technology, Brinellvägen 68, SE-10044 Stockholm, Sweden
[c] Institute for Thermal Energy Technology and Safety (ITES), Karlsruhe Institute of Technology (KIT), Hermann-von-Helmholtz-Platz 1, 76344 Eggenstein-Leopoldshafen, Germany

ABSTRACT

Reliable and cost-effective energy storage is essential to accelerate the adoption of renewable energy systems such as concentrated solar power (CSP) technologies. Single-tank Packed Bed Thermal Energy Storage (PBTES) offers a promising, lower-cost alternative to traditional two-tank systems for high-temperature storage. This study explores a hybrid sensible-latent PBTES system that integrates two types of Phase Change Materials (PCMs), strategically placed at opposite ends of a sensible-based PBTES, to enhance performance in terms of storage density and outlet fluid temperature stability. This is the first study to systematically evaluate metallic PCMs in multi-layered hybrid PBTES. A comprehensive numerical investigation, spanning PCM volume fractions from 0 to 30 % for each PCM, is conducted using a validated concentric dispersion model. The results show that PCM integration significantly boosts storage capacity, improves thermal stability, extends temperature plateaus during charging and discharging cycles and increases the energy density by up to 250 %. These hybrid configurations also extend the useful operation time by up to 220 % during charging and 300 % during discharging cycles with up to 250 % of useful energy capacity increase. Economic analysis showed a payback period of 4.8–5.5 years, with reductions in PCM layer at the top of the TES unit and encapsulation fabrication costs providing the most significant improvements in overall cost. While the hybrid system enhances temperature stability and energy utilization, it introduces trade-offs in terms of cost and efficiency, underscoring the importance of optimized PCM selection and its operating conditions. This work demonstrates the transformative potential of hybrid PBTES systems in delivering efficient, stable, and tailored energy storage solutions for future energy systems.

1. Introduction

Despite the recent dramatic drop in costs for renewable technologies like photovoltaics (PV) and concentrated solar power (CSP), they continue to face challenges, particularly energy production intermittency and the mismatch between supply and demand [1]. Thermal energy storage (TES) has emerged as a promising solution, effectively tackling these challenges in CSP plants [2–4] and other energy applications [5–7]. Nowadays, two-tank molten salt TES system currently dominates the CSP market with storage capacity ranging from 3 to 17 h [8,9]. However, several researchers have identified single-tank packed bed thermal energy storage (PBTES) as a promising alternative for

coupling with CSP plants. Implementing PBTES can lead to a promising cost reduction of around 33 % compared to the prevalent two-tank systems used for high-temperature storage [10,11].

For high-temperature applications such as CSP, liquid heat transfer fluids (HTFs) are generally preferred due to their superior heat capacity, thermal conductivity, and viscosity, which contribute to improved stratification and heat transfer coefficients in PBTES, providing substantial advantages compared to gaseous HTFs [12,13]. However, it is essential to note that many HTFs have a relatively lower maximum operating temperature limit. For example, Therminol VP-1 oil and solar salt have maximum operating temperatures of 400 °C [14] and 600 °C [15], respectively. In contrast, liquid metal HTFs [16,17] and high-temperature molten salts such as NaCl–KCl–ZnCl$_2$ [18] allow for

Nomenclature

Latin symbols

a_w	Superficial area of the storage unit per unit volume of the bed $= \pi D/A$ [m^{-1}]
h_v	Volumetric heat transfer coefficient [W m^{-3} K^{-1}]
c_p	Specific heat capacity [J kg^{-1} K^{-1}]
u_0	Fluid velocity through empty cross-sectional area [m s^{-1}]
h	Heat transfer coefficient [W m^{-2} K^{-1}]
D	Tank diameter [m]
H	Tank height [m]
L	Heat of fusion [J kg^{-1}]
T	Temperature [°C]
d	Storage medium particle diameter [m]
k	Thermal conductivity [W m^{-1} K^{-1}]
t	Time [s]
u	Fluid velocity in packed bed $u = u_0/\varepsilon$ [m s^{-1}]
x	Coordinate along tank height
y	Coordinate along particle radius
M	Material cost [$ kg^{-1}]
P	Pumping power [W]
Q_{bed}	Storage capacity of the thermal energy storage [J]
A	Cross-sectional area [m^2]
U_w	Heat transfer coefficient at tank wall [W m^{-2} K^{-1}]
V	Volume of the tank $V = \frac{\pi}{4}\left(\frac{D}{H}\right)^2 H^3$ [m^3]
M_{fab}	Encapsulation fabrication cost [$ m^{-3}]
r_e	Encapsulated PCM external radius [m]
r_i	Encapsulated PCM internal radius [m]
ut	Useful time [s]

Greek symbols

α	Thermal diffusivity $\alpha = k/(\rho c_p)$ [m^2 s^{-1}]
β	Liquid fraction
ε	Porosity
ζ	Volume fraction of a given latent heat storage medium layer

η	Efficiency [%]
μ	Dynamic viscosity [Pa s]
ρ	Density [kg m^{-3}]
ψ	Volume ratio of encapsulation material to PCM in a single capsule $\psi = \frac{(r_o^3 - r_i^3)}{r_i^3}$

Subscripts

ch	Charge
dis	Discharge
p	Storage medium particle (a sensible TES particle or a PCM capsule)
f	Fluid
ins	Instantaneous
l	Liquid
max	Maximum
min	Minimum
s	Solid
m	Melting
enc	Encapsulation

Acronyms

CSP	Concentrated solar power
CV	Control volume
HTF	Heat transfer fluid
KPI	Key performance indicator
LHTES	Latent heat thermal energy storage
PBTES	Packed bed thermal energy storage
PCM	Phase change material
PV	Photovoltaics
SOC	State of charge
TES	Thermal energy storage

Non-dimensional parameters

Bi	Biot number: $Bi = h(d/2)/k_p$
Nu	Nusselt number: $Nu = hd/k_f$
Pr	Prandtl number: $Pr = \mu_f c_{p_f}/k_f$
Re	Reynolds number: $Re = u_0 d \rho_f/\mu_f$

broader operating ranges, extending to temperatures of 800 °C or higher. Niedermeier et al. [19] compared sodium HTF to three high-temperature molten salts, finding that sodium achieved slightly higher discharge efficiency with reduced pumping requirements.

Latent heat thermal energy storage (LHTES) using phase change materials (PCMs) has attracted significant attention from the research community in recent years. In 2020, articles on LHTES made up nearly two-thirds of the total publications related to TES [20]. LHTES systems are preferred over sensible TES systems due to their higher storage density and the ability to discharge energy at an approximately constant temperature [21,22]. While single-tank PBTES systems have traditionally been categorized as sensible TES systems, recent research investigated the potential performance enhancements achieved by replacing conventional sensible storage media with encapsulated PCMs in hybrid PBTES.

The benefits of using PCM capsules instead of sensible storage media are well established in the literature. Lu et al. [23] compared sensible and PCM-based PBTES systems and found that using PCMs significantly improved the effective discharge energy compared to sensible-based PBTES. However, Yang and Cai [24] noted that this advantage comes at the cost of increased charge and discharge times due to the higher amount of stored and released energy.

To date, only a limited number of investigations have been conducted of cascaded PCM-based PBTES systems [25–29], highlighting several benefits over single-stage TES. These include operation across a wider temperature range, maintaining a more consistent temperature difference between the HTF and PCM, and achieving higher energy efficiency [30–33]. The performance of cascaded PCM-based PBTES has been investigated in various aspects, as seen in the literature. These aspects include the size of PCM particles in two-layer [26] and three-layer [27] PBTES, the heights of PCM layers [28], and the number of PCM layers, with studies examining up to five PCM layers [29].

1.1. Overview of hybrid PBTES studies

Some literature also exists on the potential advances of integrating sensible and latent TES within PBTES systems. Zhang et al. [34] investigated a hybrid TES system using paraffin PCM with natural stones to improve heat transfer. Using 3D numerical simulations, they found that granite increased the PCM melting rate by 108 % due to the enhancement of overall thermal conductivity. Through numerical modelling, Zanganeh et al. [35] proposed adding a layer of salt-based PCM capsules at the top of a sensible PBTES to stabilize the outlet temperature during the TES discharge process. Their results indicated that a PCM volume constituting only 1.33 % of the total storage volume was sufficient to achieve this purpose. Zanganeh et al. [36] experimentally validated the same concept using aluminum–silicon (Al-Si) metal alloy as PCM, demonstrating that the outflow HTF temperature remained around the melting point of the PCM for approximately 90 min. In another study, Niedermeier et al. [37] numerically investigated the benefits of partially

replacing the sensible storage medium with encapsulated Al-Si PCM. Their results demonstrated that a hybrid configuration with a 20 % PCM volume fraction could stabilize the outlet fluid temperature near the PCM melting point for approximately 18 min, accounting for about 15 % of the total discharge time.

Additionally, in two separate studies, Zhao et al. [38,39] examined the performance of multi-layered hybrid PBTES based on salt PCMs. In [39], the authors investigated the impact of hybrid PBTES configuration with various volume ratios on the capacity factor for CSP applications. In [38], they studied the effect of cut-off temperatures on the performance of an entirely sensible storage, cascaded two-layered PCM, and PCM-solid-PCM configurations. The results indicated that the hybrid configuration is preferable due to its higher capacity factor and lower cost per kWh than the fully PCM-based configuration. Galione et al. [40] reached similar conclusions, reporting that the hybrid configuration demonstrated greater efficiency than the cascaded PCM bed configuration. However, none of the existing studies on hybrid PBTES configurations have systematically explored the potential advantages of enhancing both charge and discharge temperature stability.

1.2. Research gap

While prior studies have explored hybrid PBTES systems, none have systematically analyzed the use of metallic PCMs for enhancing outlet fluid temperature stability during both charging and discharging in high-temperature applications.

1.3. Research objective

This study aims to provide a novel and comprehensive comparison between sensible and hybrid PBTES configurations that incorporate metallic PCMs. Key performance indicators (KPIs) are used to evaluate the thermal and economic performance of different design configurations.

1.4. Paper structure

This study provides a novel and comprehensive comparison of sensible and hybrid configurations, offering valuable insights into the optimal design of high-temperature thermal energy storage systems.

Section 2 details the methodology employed in this study, including the configurations studied, the selection of materials, and the KPIs. Section 3 outlines the numerical model, covering the governing equations, initial and boundary conditions, and computational methods. Section 4 focuses on model validation, comparing simulated results with experimental data from literature. Section 5 presents and discusses simulation results, highlighting key performance characteristics. Finally, Section 6 summarizes the findings and discusses their implications for designing high-temperature PBTES systems.

2. Methodology

Building on the identified research gap and objective, this section outlines the methods used to evaluate the proposed PBTES configurations. We first describe the studied storage configuration in Section 2.1, and then discuss the selection of storage medium and HTFs material for the hybrid configuration in Section 2.2. Finally, the PBTES KPIs used for evaluation are introduced in Section 2.3.

2.1. PBTES description

The PBTES system studied in this work is illustrated in Fig. 1. During the charging process, the HTF enters from the top section ($x = H$) and exits from the bottom ($x = 0$). This flow direction is reversed during the discharge phase. The analyzed PBTES system operates within a temperature range of 550 °C to 750 °C and features an 11.5 m high storage tank with a diameter-to-height ratio of 0.5, aligning with the design presented by Niedermeier et al. [19].

The design of the HTF flow rate is influenced by multiple factors, including the storage capacity, the desired charging and discharging durations, and the specific requirements of the application, particularly in relation to the integration with power conversion systems. As a result, the literature reports a broad range of HTF flow rates, reaching up to 1500 kg/s for a 100 MW CSP plant [38].

Liquid sodium is used as the HTF, flowing at a constant mass flow rate of 80 kg/s. This flow rate is double that used by Niedermeier et al. [19] to account for the larger storage capacity in the present configuration and avoid unnecessary computational time while still meeting the study's objectives. Although it is recognized that the HTF flow rate influences the overall performance of PBTES, this investigation focuses
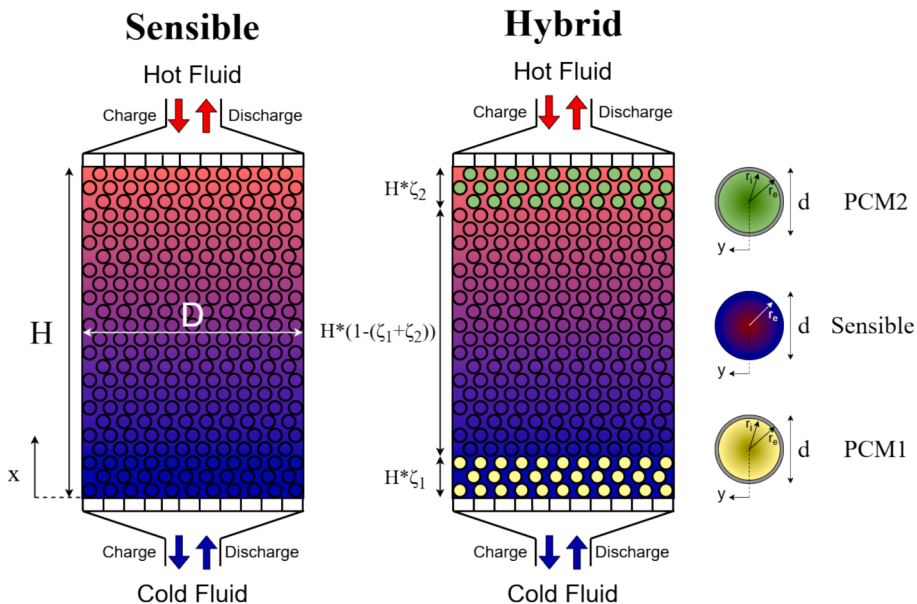

Fig. 1. Scheme of PBTES systems showing (a) conventional sensible-only configuration, and (b) hybrid sensible-latent configuration incorporating PCM layers at both ends.

exclusively on the impact of the storage medium configuration.

The storage medium, whether sensible or latent, consists of spherical particles with a uniform diameter of 50 mm. The studied range of PBTES porosity, defined as the fraction of the total volume occupied by void spaces between particles, varies from 0.3 to 0.7. The lower porosity limit of 0.3 is chosen based on the assumption of uniform particle size within the bed, as achieving porosities below 0.26 is not possible under this constraint [19]. Moreover, the upper limit of 0.7 is chosen to avoid excessive particle spacing, as it would significantly reduce storage capacity.

The PCM layers are placed at the top and bottom of the PBTES, replacing the quartzite rock in the sensible case. Through this approach, the presence of PCM layers at the bed's bottom and top, respectively allows for the stabilization of the HTF outlet temperature during the charge and discharge phases. Careful consideration should be given to the melting temperatures of the chosen PCMs to ensure optimal stabilization of the HTF outlet temperature. PCM1 should have a melting temperature slightly above the minimum operating temperature, and PCM2 should have a melting temperature just below the maximum operating temperature [41].

2.2. Storage medium and HTF material selection

In this study, uniform-sized storage medium particles with equal diameter in both the sensible and latent regions are used. The sensible filler material is a mixture of quartzite rocks and sand in a mass ratio of 2:1, similar to the work of Zhao et al. [38]. This filler combination is widely used in literature due to its good thermal properties, cost-effectiveness, and availability. The PCMs were carefully selected based on an extensive review of multiple studies [42–45] to identify the most suitable candidates for this investigation. Metallic PCMs were chosen here for their distinct advantages over salt-based alternatives, including higher thermal conductivity, long-term stability, and minimal volumetric changes during phase transitions. These properties make metallic PCMs highly appropriate for high-performance TES systems [42]. The selection of PCMs for the hybrid PBTES was guided by the following criteria:

- The material must exhibit a melting temperature appropriate for the application operating range.
- Thermophysical properties should be well-documented in literature.
- The material must maintain phase equilibrium during solid–liquid transitions.

Based on these criteria, Al-Si was selected as PCM1, and Cu-Mg-Si as PCM2. The selection of these specific metallic PCMs is primarily due to their suitable melting temperature ranges and the availability of comprehensive thermophysical property data in the literature, which is not the case for many other PCMs. Moreover, their eutectic compositions [46,47] eliminate the risk of phase separation during phase transitions, ensuring consistent thermal performance. Regarding the thermal degradation and long-term cycling effects on the latent heat and melting point, Sheng et al. [48] reported no significant change in either of them for encapsulated Al-Si PCM after 3000 melting-solidification cycles. However, the same conclusion cannot yet be drawn for Cu-Mg-Si PCM, as no detailed studies were found in the literature addressing its long-term performance under repeated thermal cycling.

In this study, the thermophysical properties for HTF are assumed to be temperature-independent. These values were calculated at an average operating temperature of 650 °C based on the formula reported by Sobolev [49]. This assumption is justified by the minimal variation in thermophysical properties of sodium within the specified temperature range. For instance, the specific heat varies by less than 1 % within the studied temperature range, with values ranging from 1253 J/(kg·K) at 750 °C to 1257 J/(kg·K) at 550 °C, based on the recommended correlation in Kirillov [50]. Additionally, the use of temperature-independent

properties for sodium across comparable temperature ranges is commonly adopted in literature, as seen in [17,19,37]. The thermophysical properties of the sensible filler, PCMs, capsule materials, and HTF are summarized in Table 1.

For encapsulating the PCMs, aluminum oxide (Al_2O_3) was chosen based on its demonstrated effectiveness in high-temperature applications, withstanding conditions up to 700 °C [51]. Al_2O_3 has been shown to provide effective corrosion resistance when in contact with both the selected PCMs and HTF. Withey et al. [52] demonstrated its compatibility with Cu–Mg–Si PCM, while Stahl et al. [53] confirmed similar resistance with Al–Si PCM. Furthermore, Courouau et al. [54] reported that Al_2O_3 is also resistant to corrosion from liquid sodium, though their study was limited to static conditions and temperatures up to 550 °C. In addition to its chemical stability, Al_2O_3 offers a relatively high thermal conductivity of 36 W/(m·K) [55], enabling efficient heat transfer between the PCM and HTF. These properties make Al_2O_3 a suitable and effective material for use in the considered high-temperature TES system.

2.3. Key performance indicators (KPIs)

In this study, several performance metrics are employed to evaluate PBTES system performance. These indicators include storage capacity, efficiency, material costs, and the stability of the HTF outlet temperature.

Energy storage capacity determines how much energy can be stored and utilized. The PBTES energy storage capacity within the operating temperature range, Q_{bed} (J), is calculated by the summation of the heat that can be stored in the materials within the storage tank and can be expressed as:

$$q = \begin{cases} \varepsilon \rho_f c_{p_f}(T_{max} - T_{min}), HTF \\ (1-\varepsilon)\rho_p c_{p_p}(T_{max} - T_{min}), sensible \\ (1-\varepsilon)\left(\rho_{s,PCM}c_{p_{s,PCM}}(T_s - T_{min})\right. \\ \quad +\dfrac{\rho_{s,PCM}+\rho_{l,PCM}}{2}L \\ \quad \left.+\rho_{l,PCM}c_{p_{l,PCM}}(T_{max} - T_l)\right), PCM1, PCM2 \end{cases} \tag{1}$$

$$Q_{bed} = V\left(q_{HTF} + \zeta_{sensible}q_{sensible} + \sum_{j=1}^{2}\zeta_{PCM_j}q_{PCM_j}\right) \tag{2}$$

In this equation, Q_{bed} (J) is the total energy that can be stored in the PBTES and q (J/m^3) represents the volume specific energy storage capacity for each region of the PBTES. The parameters T_{max} and T_{min} correspond to the maximum and minimum temperatures within the PBTES, whereas T_s and T_l (°C) represent the solidus and liquidus temperatures of PCM. The porosity of the packed bed is denoted by ε, while ρ (kg/m^3) represents the density of the storage medium. The specific heat capacity is given by c_p (J/(kg·K)), and L (J/kg) is the latent heat of fusion, relevant to phase change processes. Additionally, V (m^3) represents the total volume of the PBTES tank, and ζ denotes the volume fraction of a specific type of storage medium within the system.

In the hybrid PBTES, the subscript "f" is used to denote the fluid while the subscript "p" is used to denote the storage medium particle. Since multiple storage medium materials coexist, the particle could represent PCM1 or PCM2 in the latent heat regions or a sensible storage medium in the sensible heat region. The KPIs presented in Eq. (3) to (7) are derived from the analysis of the HTF side of the PBTES. The overall storage efficiency η can be calculated by comparing the recovered energy during discharge to the energy input during the charge as follows:

$$\eta = \frac{Q_{recovered}}{Q_{input}} = \frac{\int_0^{t_{dis}} \dot{m}c_{p_f}(T|_{x=H}(t) - T_{min})dt}{\int_0^{t_{ch}} \dot{m}c_{p_f}(T_{max} - T_{min})dt} \tag{3}$$

Table 1

Thermophysical properties and material cost of HTF and storage medium materials used.

	Property	Unit	HTF	Sensible storage medium	Encapsulation	PCM1	PCM2
Name			Sodium	Sand + Quartzite rocks	Aluminum Oxide	Aluminum-silicon alloy	Copper-magnesium-silicon alloy
Formula			Na	SiO_2	Al_2O_3	Al-Si (Wt%88:12)	Cu-Mg-Si (Wt%56:17:27)
Sources			[49,56]	[38,57]	[38,55,58]	[7,59,60,61]	[62,63]
	T_m	°C	–	–	–	575	742
	ρ_s	kg m^{-3}	–	2500	3890	2620	5060
	ρ_l	kg m^{-3}	791	–	–	2579	3200
	c_{p_s}	J kg^{-1} K^{-1}	–	830	–	1300	750
	c_{p_l}	J kg^{-1} K^{-1}	1251.3	–	–	1100	634.6*
	k_s	W m^{-1} K^{-1}	–	5.69	36	181	150
	k_l	W m^{-1} K^{-1}	60	–	–	63	52.2*
	μ	mPa s	0.2	–	–	–	–
	L	J kg^{-1}	–	–	–	481,000	423,000
	M	\$ kg^{-1}	2	0.013	0.75, M_{fab}**	1.4	5.6

* Calculated based on the same solid–liquid property values ratio of Al-Si PCM.

** M_{fab} = 44640 (\$/m^3) is the encapsulation fabrication/manufacturing cost in as indicated in[64].

Here, $\dot{m}$ (kg/s) represents the fluid mass flow rate, and T (°C) denotes the fluid temperature at a specified location. The integration limits, t_{ch} and t_{dis} (s) correspond to the time required to complete the full charging and discharging cycles, respectively.

Maintaining a stable outlet temperature is crucial for ensuring that downstream processes receive a consistent and dependable heat supply during discharge. In power generation, temperature fluctuations can result in inefficiencies or even cause damage to equipment. Additionally, a stable outlet temperature during the charging phase is essential to fully utilize available energy sources, minimizing energy losses, as seen in CSP fields. Here, the KPI useful time (*ut*) is identified, which represents the charge or discharge time (Δt) respectively at which the outlet HTF temperature remains within a desirable temperature range (threshold). This desirable temperature value is identified to be below $T_{min} + 40$ °C for charging and above $T_{max} - 40$ °C during discharging, based on 20 % allowed temperature change suggested by Modi and Pérez-Segarra [65].

$$Useful\ time(ut) = \begin{cases} \Delta t(T|_{x=0} < 590°C), charge \\ \Delta t(T|_{x=H} > 710°C), discharge \end{cases} \quad (4)$$

Efficiency primarily focuses on the quantity of energy stored or released; however, in this study, the utilization ratio is also considered. The utilization ratio represents the amount of energy stored or released within the useful time compared to the total energy, providing a more comprehensive assessment of the system's performance.

$$Utilization\ ratio = \begin{cases} \dfrac{\int_0^{t_{ut}} \dot{m}c_{p_f}\left(T|_{x=0}(t) - T_{min}\right)dt}{\int_0^{t_{ch}} \dot{m}c_{p_f}\left(T|_{x=0}(t) - T_{min}\right)dt}, charge \\ \dfrac{\int_0^{t_{ut}} \dot{m}c_{p_f}\left(T|_{x=H}(t) - T_{min}\right)dt}{\int_0^{t_{dis}} \dot{m}c_{p_f}\left(T|_{x=H}(t) - T_{min}\right)dt}, discharge \end{cases} \quad (5)$$

Further, the charging and discharging thermal power of the PBTES, P_{bed}, can be calculated with the following equation:

$$P_{bed} = \begin{cases} \dot{m}c_{p_f}\left(T_{max} - T|_{x=0}(t)\right), charge \\ \dot{m}c_{p_f}\left(T|_{x=H}(t) - T_{min}\right), discharge \end{cases} \quad (6)$$

Where P_{bed} (W) is the thermal power of charging or discharging the PBTES. The state of charge (SOC) during charging and discharging is defined as:

$$SOC = \begin{cases} \dfrac{\int_0^{t} \dot{m}c_{p_f}\left(T|_{x=0}(t) - T_{min}\right)dt}{\int_0^{t_{ch}} \dot{m}c_{p_f}\left(T|_{x=0}(t) - T_{min}\right)dt}, charge \\ \dfrac{\int_0^{t} \dot{m}c_{p_f}\left(T|_{x=H}(t) - T_{min}\right)dt}{\int_0^{t_{dis}} \dot{m}c_{p_f}\left(T|_{x=H}(t) - T_{min}\right)dt}, discharge \end{cases} \quad (7)$$

Essentially, the dominator of the SOC is the PBTES storage capacity Q_{bed} minus the heat loss to ambience.

The cost estimation of sensible-based PBTES is based on Niedermeier et al. [19]. In this study, the cost equation has been generalized to accommodate any storage configuration, whether fully sensible, hybrid, or completely latent. The modified equation incorporates additional factors, such as the costs associated with PCM encapsulation materials and fabrication, when PCM layers are present. This cost formulation exclusively considers the contributions of the storage medium materials and the HTF, while excluding financial factors related to the tank material, foundation, insulation, and auxiliary components such as pumps, piping, and distributors.

$$Storage\ cost\ (\$/kWh) = \frac{(Term\ 1 + Term\ 2)}{\left(q_{HTF} + q_{sensible} + \sum_{j=1}^{2} \zeta_{PCM_j} q_{PCM_j}\right)} \quad (8)$$

$$where$$
$$Term\ 1 = \varepsilon\rho_f M_f + \zeta_{sensible}(1-\varepsilon)\rho_p M_p$$
$$Term\ 2 = \sum_{j=1}^{2} \zeta_{PCM_j}(1-\varepsilon)\left[\rho_p M_p + \psi_{enc}\left(M_{fab} + \rho_{enc}M_{enc}\right)\right]$$

Where ψ_{enc} is the ratio of encapsulation volume to PCM volume, $M(\$/kg)$ is the mass specific material cost, and M_{fab} (\$/m^3) is the volumetric specific fabrication cost. Moreover, q values are calculated based on Eq. (1).

3. Model description

To implement the outlined methodology, a detailed numerical model was developed to simulate the thermal behavior of the PBTES system. The following chapter provides a comprehensive description of the model geometry, governing equations, and boundary conditions. It begins with the governing equations outlined in Section 3.1, followed by the initial and boundary conditions in Section 3.2. Convective heat transfer coefficient formulation is discussed in Section 3.3, while Section 3.4 covers the spatial and temporal discretization schemes. Finally, Section 3.5 addresses the grid and time step sensitivity analyses.

To capture the thermal behavior of the packed bed during charging and discharging cycles, the model accounts for transient heat transfer, fluid flow through porous media, and phase change of the PCM. The governing energy equations for the fluid and storage media domains are provided in Eq. (9) and Eq. (11), respectively. The initial condition is defined in Eq. (16), while the boundary conditions are detailed in Eq. (17) through Eq. (21). The treatment of the PCM's thermophysical properties is described in Eq. (13) to Eq. (15), and the evaluation of the heat transfer coefficient is outlined in Eq. (22) through Eq. (24).

3.1. Governing equations

Several numerical models have been developed to analyze PBTES systems in the literature, including the single-phase model, Schumann's model, the continuous solid-phase model, and the concentric dispersion model. For a more detailed discussion of these models, refer to [66–70]. Among these, Schumann's model is widely adopted; however, it neglects internal temperature gradients within the storage medium particles, which limits its applicability in systems involving phase change. In contrast, the concentric dispersion model resolves the internal thermal gradients within the storage particles, making it more appropriate for the hybrid PBTES configuration investigated in this study. Although computationally more demanding, this model allows for accurate representation of the PCM phase change process by capturing the internal temperature evolution within the encapsulated PCM [69], thereby providing a more realistic simulation of heat transfer dynamics.

The governing equations for each domain in this study are adopted from Ismail and Stuginsky [66]. The energy equation for the HTF domain can be expressed as:

$$\varepsilon \rho_f c_{p_f} \left(\frac{\partial T}{\partial t} + u \frac{\partial T}{\partial x} \right) = \varepsilon k_f \frac{\partial^2 T}{\partial x^2} + h_v \left(T_p \big|_{y=r_e} - T \right) - U_w a_w (T - T_\infty) \tag{9}$$

Where u (m/s) represents the fluid velocity, while k (W/m·K) is the thermal conductivity, h_v (W/m³·K) is the volumetric heat transfer coefficient. The heat loss term parameters U_w (W/m²·K), a_w (1/m) and T_∞ (°C) refer to the overall heat transfer coefficient of the tank, the superficial area of the storage unit per unit volume of the bed, the ambient temperature which is assumed to be 25 °C, respectively.

Thermal losses to the external environment involve several heat transfer mechanisms: convection at the internal and external surfaces of the tank. This involves heat exchange between the tank and fluid at the internal surface and between the tank and the environment at the external surface. Also, heat is transferred by conduction through the tank's material and insulation layer. These combined processes contribute to U_w as defined by the Eq. (10) [71]. The convective heat transfer coefficients h_{inside} and $h_{outside}$ (W/m²·K) are calculated based on formulas obtained from Beek [72] and Ismail and Stuginsky [66], respectively.

$$\frac{1}{U_w} = \frac{1}{h_{inside}} + \frac{D}{2} \sum_{j=1}^{n} \frac{1}{k_j} \ln \frac{D_{j+1}}{D_j} + \frac{1}{h_{outside}} \frac{D_{outside}}{D_{ins}} \tag{10}$$

The model excludes heat storage within the tank wall to reduce the computational cost. Hoffmann et al. [73] recommend this assumption when the heat stored in the tank wall comprises less than 5 % of the total thermal energy storage capacity. For the cases considered here, this threshold is met in all instances. Additionally, intra-particle diffusion can be accounted for by using the energy equation for a single representative storage medium particle, as provided in Eq. (11).

$$\rho_p c_{p_p} \frac{\partial T_p}{\partial t} = k_p \left(\frac{\partial T_p^2}{\partial y^2} + \frac{2}{y} \frac{\partial T_p}{\partial y} \right) \tag{11}$$

The storage medium thermophysical properties are listed in Table 1. While a single property value is used for the sensible heat region, the property values in the latent heat regions vary depending on the phase of the PCM. The liquid fraction of the PCM, β, is determined based on the temperature of the control volume (CV), following the approach outlined by Galione et al. [40], as follows:

$$\beta = \begin{cases} 0, T_{PCM} \leq T_{solidus} \\ 1, T_{PCM} \geq T_{liquidus} \\ \dfrac{T_{PCM} - T_{solidus}}{T_{liquidus} - T_{solidus}}, T_{solidus} < T_{PCM} < T_{liquidus} \end{cases} \tag{12}$$

The density and thermal conductivity of the PCM are handled as described in Eq. (13) and Eq. (14). While constant values are used for the solid and liquid phases of the PCM, an average of the solidus and liquidus properties is applied during the PCM phase transition ($0 < \beta < 1$).

$$\rho_{PCM} = \begin{cases} \rho_s, T_{PCM} \leq T_{solidus} \\ \rho_l, T_{PCM} \geq T_{liquidus} \\ \dfrac{\rho_s + \rho_l}{2}, T_{solidus} < T_{PCM} < T_{liquidus} \end{cases} \tag{13}$$

$$k_{PCM} = \begin{cases} k_s, T_{PCM} \leq T_{solidus} \\ k_l, T_{PCM} \geq T_{liquidus} \\ \dfrac{k_s + k_l}{2}, T_{solidus} < T_{PCM} < T_{liquidus} \end{cases} \tag{14}$$

The effective heat capacity approach [26,74–76] is utilized to account for the phase change in the PCM. It is important to highlight that this method relies on a defined temperature range for the phase change [77], which makes it unsuitable for materials with coinciding solidus and liquidus temperatures, such as eutectic alloys.

$$c_{p_{PCM}} = \begin{cases} c_{p_s}, T_{PCM} \leq T_{solidus} \\ c_{p_l}, T_{PCM} \geq T_{liquidus} \\ \dfrac{c_{p_s} + c_{p_l}}{2} + \dfrac{L}{\Delta T_m}, T_{solidus} < T_{PCM} < T_{liquidus} \end{cases} \tag{15}$$

3.2. Initial and boundary conditions

At the beginning of charge and discharge scenarios, a uniform temperature is assumed across the entire computational domain, encompassing both the HTF and storage medium materials. During the charge phase, this temperature is set to the minimum operating temperature, while in the discharge phase, the temperature is set to the maximum operating temperature.

$$t = 0 : \begin{cases} T(x) = T_p(x,y) = T_{min}, charge \\ T(x) = T_p(x,y) = T_{max}, discharge \end{cases} \tag{16}$$

At both ends of the tank, it is assumed that the storage medium material does not transfer energy at the inlet or the outlet. A fixed temperature boundary condition is applied at the HTF inlet, while a zero-heat flux condition is imposed at the HTF outlet.

$$charge : \begin{cases} \dfrac{\partial T}{\partial x} = 0, \dfrac{\partial T_p}{\partial x} = 0, x = 0 \\ T_{in} = T_{max}, \dfrac{\partial T_p}{\partial x} = 0, x = H \end{cases} \tag{17}$$

$$discharge : \begin{cases} T_{in} = T_{min}, \dfrac{\partial T_p}{\partial x} = 0, x = 0 \\ \dfrac{\partial T}{\partial x} = 0, \dfrac{\partial T_p}{\partial x} = 0, x = H \end{cases} \tag{18}$$

Further boundary conditions include a symmetry condition at the center of the particle and a convection boundary condition at the outer surface of the particles. The symmetry condition is applied for all storage medium particles and can be described as:

$$y = 0 : \frac{\partial T_p}{\partial y} = 0 \tag{19}$$

However, the convection boundary condition may vary depending on the type of storage medium. For the sensible heat region, the following boundary condition is applied [41,78]:

$$y = r_e : -k_p \frac{\partial T_p}{\partial y} = h(T_p - T) \tag{20}$$

For the latent heat sections, the convection boundary condition is adjusted to consider the thickness and thermal conductivity of the PCM capsule shell, following the approach described by Ismail and Henriquez [79].

$$y = r_e : -k_p \frac{\partial T_p}{\partial y} = \frac{(T_p - T)}{\left(\frac{(r_e - r_i)}{k_{enc}} \left(\frac{r_i}{r_e} \right) + \left(\frac{r_i}{r_e} \right)^2 \left(\frac{1}{h} \right) \right)} \tag{21}$$

3.3. Heat transfer between fluid and storage medium particles

The heat transfer coefficient h between the fluid and the particles, along with the volumetric heat transfer coefficient h_v used in the fluid energy equation, can be expressed as follows [80]:

$$h = \frac{Nuk_f}{d} \tag{22}$$

$$h_v = h \frac{6(1 - \varepsilon)}{d} \tag{23}$$

Where d (m^2) is the storage medium particle diameter.

Oró et al. [81] compared various Nusselt number (Nu) correlations from sources [82,83], and [84] and found that they all produced similar temperature profiles within the PBTES for the studied case. As a result, they concluded that any of these correlations can be used. Despite that, in the correlation by Wakao et al. [83], which is widely used in the literature [85–87], attention should be given to the selection of appropriate Nu correlation when dealing with HTFs with very low Prandtl numbers (*Pr*), such as sodium. This is expected to be addressed through the investigation of Schmidt et al. [88] but the results are not published yet. Therefore, the correlation of Melissari and Argyropolus [89], which has been found for a single sphere for a wide range of *Pr* within the range between 0.003 and 10, is implemented as follows:

$$Nu = 2 + 0.47Re^{1/2}Pr^{0.6} \tag{24}$$

3.4. Solution procedure

Utilizing the mathematical model explained in Section 3.1, the governing equations were solved in Matlab using the finite volume approximation. The computational resources utilized for the simulation include an Intel® Xeon® Silver 4214R CPU @ 2.4 GHz, equipped with 24 processors and 96 GB of RAM. Temporal discretization was performed using the forward Euler method explicit scheme as in Zanganeh et al. [36]. For spatial discretization, the first-order upwind scheme was applied to the advection terms, while the second-order central difference scheme was used for the diffusion terms, similar to ELSihy et al. [41]. The model is based on the following assumptions:

- One-dimensional HTF flow and temperature distribution (in the vertical direction).
- One-dimensional temperature distribution within the storage medium particles (radial direction).
- The liquid fraction changes linearly with the temperature.
- Natural convection, volume change, and contact melting within the PCM capsules are disregarded, and radiation heat transfer is considered negligible.
- The storage medium particles' shape is spherical, and the dual-media (HTF and storage medium) zone is treated as a homogeneous isotropic region with the same porosity throughout the tank.
- For all PCMs, the phase transition occurs over a temperature range of 4 °C ($\Delta T_m = 4$ °C), during which the material exhibits a high specific heat capacity.

- The heat stored or released by the PCM capsule shell is considered negligible, with only the thermal resistance of the shell taken into account.

3.5. Spatial and temporal discretization sensitivity

To assess the impact of spatial discretization on the solution, three different grids were used in both the axial and radial directions for each case. All grid optimization studies were conducted with a time step of 0.002 s. The HTF temperature at three different axial positions was recorded for each grid. The results, displayed in Fig. 2, show that a grid configuration of 400 CVs in the axial direction of the PBTES and 30 CVs in the radial direction of the storage medium particle yields results comparable to those from a finer grid, with a computational time savings of 50 % in the axial direction and 34 % in the radial direction, as detailed in Table 2.

Regarding temporal discretization, three different time step sizes were tested. Given the conditional stability of explicit schemes, a stability criterion is applied to the temporal discretization to maintain numerical stability. In each simulation, the time step is ensured to satisfy the $dt \leq minimum \left(\frac{(dx)^2}{\alpha_f}, \frac{(dy)^2}{\alpha_p} \right)$ criterion, accounting for both axial and radial directions, as the diffusion terms impose a more restrictive limit than the advection terms. The simulation results demonstrated that applying a time step within the range of 0.0005 and 0.002 s produced almost no variations in the solution. The largest time step found to maintain numerical stability and solution accuracy in all studied grids is 0.002 s. Based on this sensitivity analysis, further simulations are conducted using a grid size of (400 × 30) with a time step of 0.002 s.

4. Model validation

With the numerical model established, the next step involves validating its accuracy by comparing simulation results against benchmark cases and relevant experimental data, as detailed in the following chapter. Since this work addresses both sensible and latent TES, the model is validated separately against experimental data for each type. Table 3 presents a detailed summary of the conditions for the validated cases.

Firstly, the laboratory-scale experiment conducted at the PROMES-CNRS laboratory and reported by Hoffmann et al. [73] is considered. This prototype utilized rapeseed oil as the HTF and quartzite rocks as the sensible heat storage medium, featuring a porosity of 0.41 and operating within a temperature range of 160 °C to 210 °C. The experimental and numerical temperature distribution along the tank axis shown in Fig. 3 (a) are in quite good agreement with t = 1, 2, and 3 h discharge time, taking into consideration ± 10 % uncertainty in the experiment's flow measurements.

The second validation study involves the experiment reported by Nallusamy et al. [90]. In this study, the authors investigated the thermal behavior of a latent heat PBTES system designed for solar collector applications. Spherical capsules containing paraffin PCM with a melting temperature range of 59 °C to 61 °C were used to fill the tank, which had a void fraction of 0.369. The experiments were conducted with a constant inlet water HTF at temperatures of 70 °C and 66 °C, with a flow rate of 2 L per minute. The fluid temperature at an axial position of x/H = 0.5 was recorded for both inlet temperatures throughout the charging period. Fig. 3 (b) demonstrates that our model accurately predicts the fluid temperature for both inlet fluid temperatures throughout the entire duration.

In the third validation study, the results reported by Niedermeier et al. [19] were reproduced to verify the model's accuracy for a discharge case of a high-temperature sensible heat PBTES system operating between 500 and 700 °C. The system employs quartzite rocks (with a particle diameter of 0.015 m) as the storage medium, featuring a
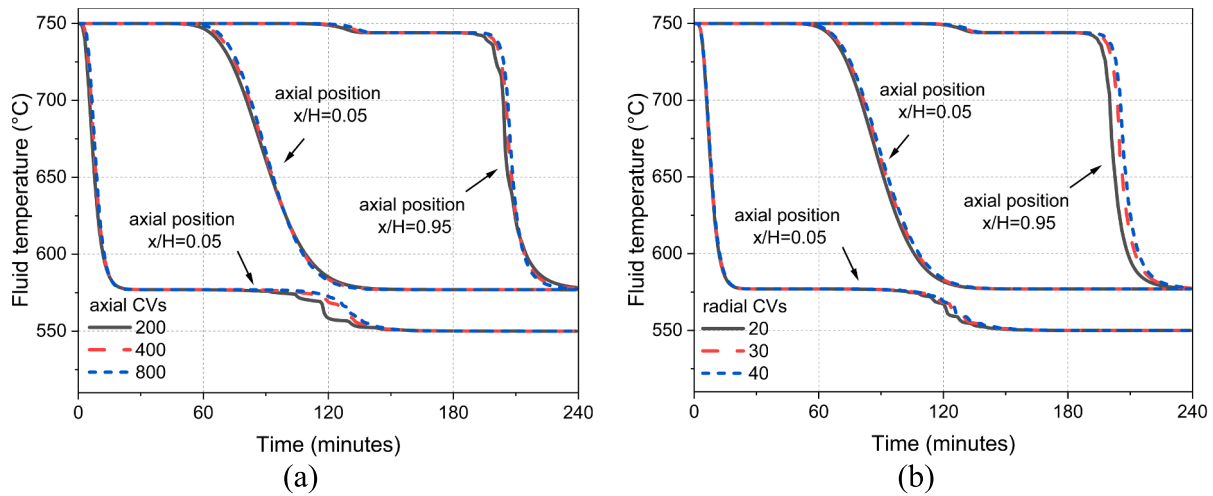
Fig. 2. Temperature profile at different axial locations for different grid sizes in (a) axial direction and (b) radial direction.

Table 2
Computation time for varying spatial discretization and time step sizes.

	Value	Time (min)
# of CVs in the tank axial direction	200	24
	400	46
	800	91
# of CVs in the particle radial direction	20	24
	30	44
	40	67
Time step size (s)	0.0005	233
	0.001	119
	0.002	58

porosity of 0.22, and uses a $ZnCl_2$-NaCl-KCl chloride salt mixture as HTF. As shown in Fig. 3 (c), the predictions from the current study successfully replicate the fluid temperature profiles at various stages of discharge (t = 1, 2, 3, and 4 h), with only minimal discrepancies observed.

The validation studies confirm that the model effectively represents the temperature in the PBTES system for both sensible and latent heat scenarios. This is supported by quantitative error metrics such as Mean Absolute Error (MAE) and Relative Mean Square Error (rMSE) values, which are below 3.5 K and $1.4 \cdot 10^{-4}$, respectively, across all validation cases. These small error values are within the acceptable limits as per previous studies, e.g., Niedermeier et al. [19] and Hoffmann et al. [73]. Therefore, the model can be confidently utilized for further analysis.

5. Results and discussions

Based on the validated model and simulation parameters, this section presents the performance results of sensible and hybrid PBTES configurations, highlighting key thermal and economic outcomes. Section 5.1 examines the energy storage density and the role of PCMs, while Section 5.2 presents the temperature profiles during charging and discharging within the PBTES. Section 5.3 discusses the stability of the outlet HTF temperature, and section 5.4 analyzes the thermal power behavior during energy storage and release. Section 5.5 highlights the results of a parametric study across a wide range of PCM volume fractions, identifying optimal configurations and the trade-offs between competing objectives. Section 5.6 investigates the effects of temperature gradients between the inlet fluid and PCM melting point on system performance. Finally, preliminary cost analysis is presented in section 5.7.

5.1. Storage capacity

The increase in storage capacity with higher PCM volume fractions, as shown in Fig. 4 ($\varepsilon = 0.5$), is a direct result of the latent heat of fusion, which enables greater energy density compared to the fully sensible configuration. In the fully sensible case ($\zeta_1 = \zeta_2 = 0$ %), the total storage capacity is limited to approximately 25 MWh, contributed solely by the sensible material and the HTF. As the PCM1 and PCM2 volume fractions increase, the overall storage capacity rises significantly due to the latent heat contributions of the PCMs. For a configuration with $\zeta_1 = \zeta_2 = 30$ %, where PCMs dominate the storage medium while the remaining 40 % consists of sensible material, the total storage capacity exceeds 60 MWh. This corresponds to an energy density increase of approximately 250 % compared to the fully sensible configuration for the given geometry and volume. It is also worth noting that, although PCM2 exhibits a lower latent heat per kilogram than PCM1, its total energy contribution is greater. This is primarily due to its higher density, which compensates for the lower specific latent heat, further increasing the overall storage capacity of the system.

Porosity (ε) is defined as the ratio of the void volume, occupied by the HTF, to the total volume of the packed bed. In the simulations, ε was treated as an input parameter used to determine the solid and fluid volume ratios within each control volume. This parameter influences both the thermal and economic performance of the system. For instance, porosity directly impacts the storage capacity (Eq. (1)), the volumetric heat transfer coefficient (Eq. (23)), and the estimated storage cost (Eq. (8)), thereby playing a key role in the overall behavior and economics of the PBTES system.

The effect of porosity on the storage capacity of PBTES is shown in Fig. 5 for two configurations: a fully sensible configuration and a hybrid configuration with $\zeta_1 = \zeta_2 = 10$ %. The investigated porosity range spans from 0.3 to 0.7. The results clearly indicate that the hybrid configuration consistently achieves a higher storage capacity than the fully sensible configuration across all porosity levels. While the differences between the two configurations become less pronounced at higher porosity values, the hybrid configuration demonstrates a substantial advantage at lower porosity. Specifically, when the storage medium particles density is higher (low porosity), the storage capacity in the hybrid configuration exceeds that of the sensible configuration by approximately 20 MWh. The difference in storage capacity between the sensible and hybrid configurations becomes even more significant at higher PCM percentages.

Table 3
Summary of model inputs for validating HTF temperature profiles.

Parameter	Validation study		
	1(experimental)	2(experimental)	3(numerical)
Storage medium type	Sensible	Latent	Sensible
Reference study	[73]	[90]	[19]
System operation			
Charge/Discharge	Discharge	Charge	Discharge
Total simulation time, min	180	240	240
HTF type	Rapeseed oil	Water	ZnCl$_2$-NaCl-KCl chloride salt
Storage medium particles type	Quartzite rocks	Paraffin PCM	Quartzite rocks
Fluid velocity through the empty cross-sectional area, mm s^{-1}	0.237	0.327	1.1
Temperature operating range, °C (T_{min}/T_{max})	160 / 210	32 / 70	500 / 700
		32 / 66	
Size			
Height of packed bed, m	1.8	0.46	11.3
Tank diameter-to-height ratio	0.22	0.78	0.5
Diameter of sensible storage medium/PCM capsules, mm	40	55	15
Porosity	0.41	0.369	0.22
Thermal properties			
Phase change temperature range, °C	–	59–61	–
Latent Heat of PCM, J kg^{-1}	–	213,000	–
Density, kg m^{-3}			
For HTF	638	983.2	1977
For storage medium particles	2640	861(s) / 778(l)	2640
Specific heat, J kg^{-1} K^{-1}			
For HTF	2651	4182	900
For storage medium particles	1050	1850(s) / 2384(l)	1050
Thermal conductivity, W m^{-1} K^{-1}			
For HTF	0.2815	0.653	0.29
For storage medium particles	2.5	0.4(s) / 0.15(l)	2.5
Discretization details			
Time step, s	0.1	0.01	0.01
CV$_S$ Number (packed bed × storage medium particle)	100 × 20	100 × 50	400 × 20
Error calculations			
Mean Absolute Error (MAE), $KMAE = 1/n \sum \left(T_{ref} - T\right)$	2.7	1.3	3.5
Relative Mean Square Error (rMSE) $rMSE = 1/n \sum \left(\frac{T_{ref} - T}{T_{ref}}\right)^2$	5.7·10^{-5}	4.3·10^{-5}	1.4·10^{-4}

5.2. HTF temperature profiles in the PBTES

The distribution of the fluid temperature within the PBTES is comprehensively analyzed in this study. Fig. 6 provides a comparison between two configurations: one consisting entirely of sensible filler material and another utilizing a hybrid design with PCM layers occupying $\zeta_1 = \zeta_2 = 10$ % of the bed height, with the remaining 80 % comprising sensible filler. Both configurations are studied for charging and discharging processes.

In the fully sensible configuration (i.e., Fig. 6 (a) and (b)), the temperature profiles exhibit a distinct thermocline that progresses upward during charging and downward during discharging, reflecting efficient heat transfer and well-preserved thermal stratification. In contrast, the hybrid configuration (i.e., Fig. 6 (c) and (d)) demonstrates a more complex behavior due to the incorporation of PCM layers.

The hybrid configuration requires longer charging and discharging times, primarily due to the increased storage capacity (thus more thermal inertia) introduced by the latent heat of the PCM and the lower temperature difference between the fluid and fillers at later stages (thus a lower driving force for heat transfer). Notably, during the charge and discharge cycles, the HTF temperature stabilizes at approximately 742 °C and 575 °C. These plateaus, evident in Fig. 6 (d), are directly linked to the melting temperatures of PCM2 (742 °C) and PCM1 (575 °C).

The upper plateau at x/H = 0.95 corresponds to the PCM2 layer, where the latent heat of fusion is absorbed or released during the phase transition. Similarly, the lower plateau, observed across all profiles, results from the melting temperature of PCM1. For instance, at x/H = 0.05, the stabilization at 575 °C is directly attributable to the PCM1 region, where phase change occurs. The temperature stabilization in other regions is indirectly influenced by the time delay of HTF exiting

PCM1 and traveling through the bed, as well as the residual heat stored within the filler materials at temperatures between 550 °C and 575 °C. A similar pattern can be observed in Fig. 6 (c) during the charging process, though in a reversed manner.

5.3. HTF outlet temperature stability

Based on the threshold criteria outlined in section 2.3, the temperature thresholds are set at 590 °C for the charging scenario and 710 °C for the discharging scenario. Fig. 7 highlights the advantages of the hybrid configuration in stabilizing the outlet fluid temperature for an extended duration during both charging and discharging processes, compared to the fully sensible configuration. The temperature plateaus observed in the hybrid configuration are a direct consequence of the nearly isothermal heat storage and release associated with the PCMs at their respective melting points. These plateaus, which enhance temperature stability, are analyzed in greater detail in section 5.2.

The sharp transitions observed in the charging and discharging curves of the hybrid configuration are attributed to the significant temperature difference between the PCM layers (which maintain a stable temperature near their melting points) and the HTF entering the sections. This behavior occurs because the sensible heat regions charge or discharge faster than the latent heat regions in the PCM layers. As the phase change process concludes, the PCM layers also shift to sensible heat addition or rejection, causing the outlet temperature to rise or drop sharply.

Additionally, the shorter discharge time compared to the charging time can be explained by the higher temperature difference between the PCM1 melting point and the HTF inlet temperature during discharge. This larger temperature gradient facilitates more efficient heat transfer during the discharge process. Conversely, the lower temperature
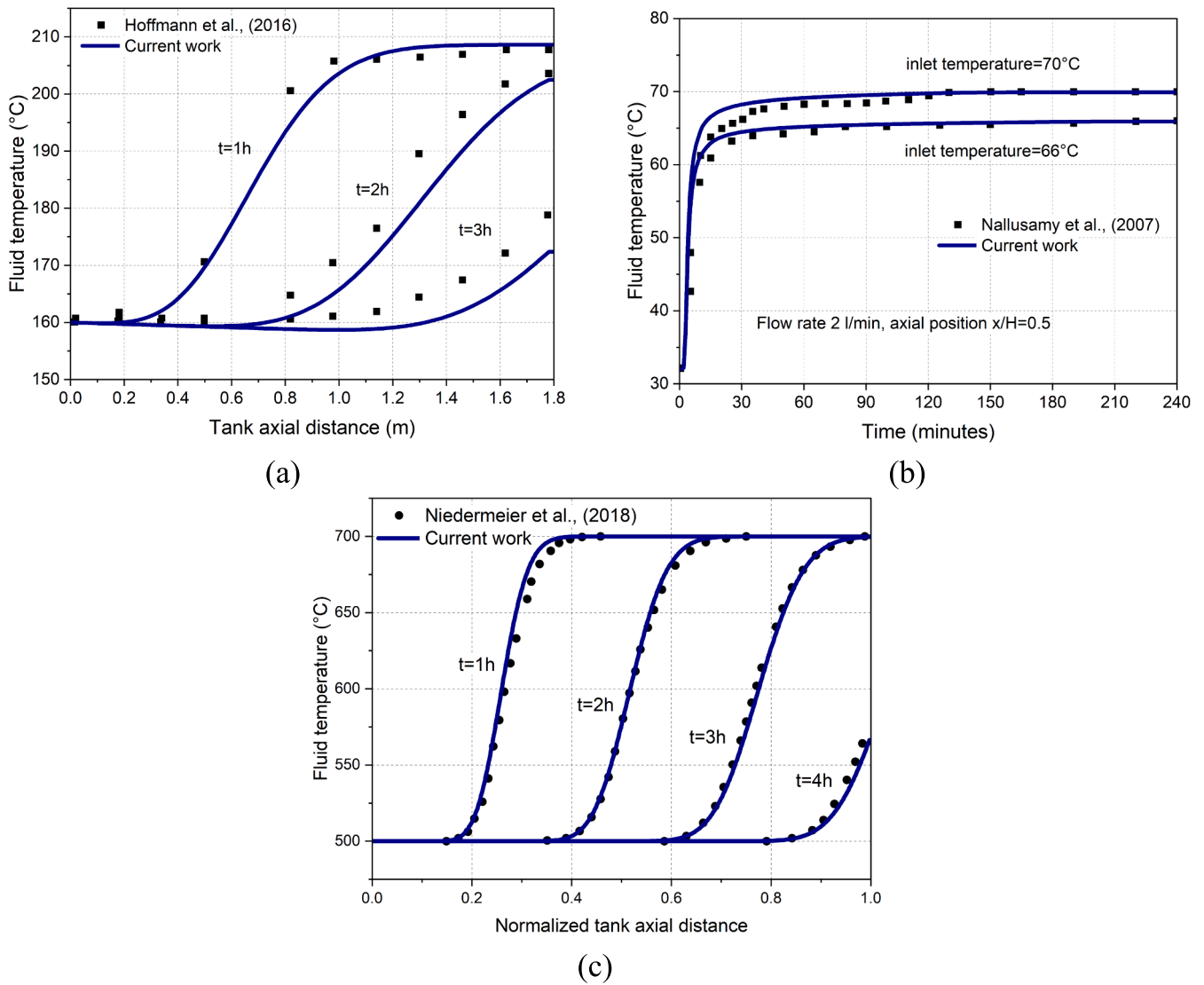
(a)

(b)

(c)

Fig. 3. Comparison of predicted and reported HTF temperature profiles in the literature for PBTES systems, (a) for sensible heat [73], (b) for latent heat [90], and (c) high-temperature sensible heat [19].

difference during charging reduces the heat transfer efficiency between the HTF and PCM2, leading to prolonged charging times and lower overall efficiency. The impact of this reduced efficiency is discussed in section 5.5, while a detailed sensitivity analysis addressing these issues is presented in section 5.6.

Fig. 8 summarizes the time during which the outlet fluid temperature remains within the desirable temperature range for various configurations of hybrid PBTES systems, with different volume fractions of PCM1 and PCM2 (ζ_1, ζ_2) and porosities. Both charging and discharging processes are evaluated to highlight the influence of increasing PCM volume fractions on system performance.

For the fully sensible configuration ($\zeta_1=\zeta_2=0\%$), the desirable outlet temperature range is maintained for approximately 60 min during both charging and discharging. With the addition of PCM layers, this duration increases significantly, reaching an improvement of 220 % during charging and 300 % during discharging for the configuration with $\zeta_1 = \zeta_2 = 30\%$ volume fraction, for $\varepsilon = 0.3$ for instance. This trend indicates that incorporating PCMs prolongs useful time and hence energy storage capacity during charging and discharging due to the latent heat storage in the PCM layers.

The observed disparity in useful times between charging and discharging is attributed to the differing thermophysical properties of

PCM1 and PCM2. PCM2, with its substantially higher density, has greater mass to undergo phase change, contributing to prolonged stabilization of the outlet temperature during discharging compared to charging. This underlines the role of PCM2 in enhancing system performance of the application, particularly during the discharging cycle.

These results demonstrate the critical role of PCM volume fraction in enhancing the thermal performance of hybrid TES systems, particularly for applications requiring prolonged temperature stability.

5.4. Charge and discharge thermal power

Fig. 9 presents the thermal power curves as a function of the SOC for both charging and discharging processes, comparing the sensible configuration and a hybrid configuration ($\zeta_1 = \zeta_2 = 10\%$). During the charging process, the thermal power in the sensible configuration remains near its maximum value of approximately 20 MW until reaching an SOC of 0.7, after which it begins to decline. In contrast, the hybrid configuration exhibits an earlier drop in power, stabilizing at around 17 MW within the SOC range of 0.61 to 0.78. This stabilization corresponds to the phase change occurring in the PCM1 layer. Once the PCM1 layer is almost fully molten, the thermal power in the hybrid configuration decreases more sharply compared to the sensible configuration. This is
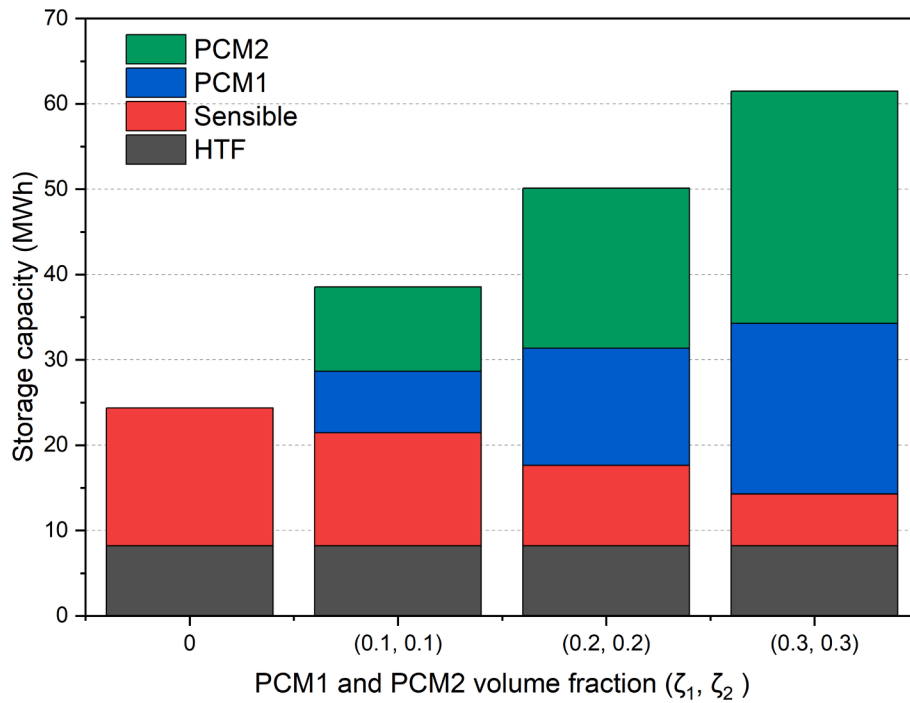
Fig. 4. Storage capacity breakdown by TES components for different PCM volume fractions.
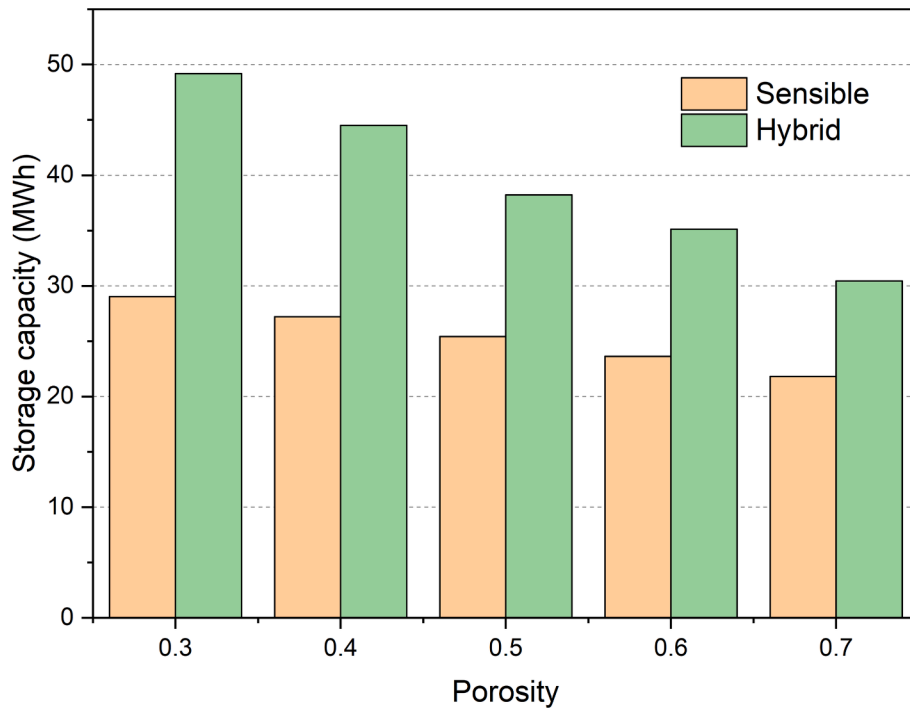

Fig. 5. Storage capacity comparison between sensible and hybrid configurations for varying porosities.

confirmed by the liquid fraction contour (x/H = 0.09) shown in Fig. 10 (a), where the final PCM1 layer is fully melted at a SOC value of approximately 0.8. Additionally, a second plateau appears beyond an SOC of 0.81 in the hybrid curve, indicating that the PCM2 layer is still undergoing its melting process.

During the discharging process, the thermal power curves again reveal significant differences between the sensible and hybrid configurations. Although the general behavior of the curves resembles those observed during charging, especially for the sensible configuration, key

distinctions are evident. In the hybrid configuration, the power stabilizes over a broader SOC range at approximately 19 MW for a longer portion of the process, and at 2.5 MW for a shorter duration, compared to the charging phase. This is attributed to the higher heat content in the PCM2 layer compared to PCM1.

A deeper analysis of the melting and solidification of the PCM layers of a hybrid configuration ($\zeta_1 = \zeta_2 = 10$ %) is conducted. Fig. 10 represents the liquid fraction of both PCMs at three different locations for each PCM layer, plotted against SOC. The SOC also indirectly represents
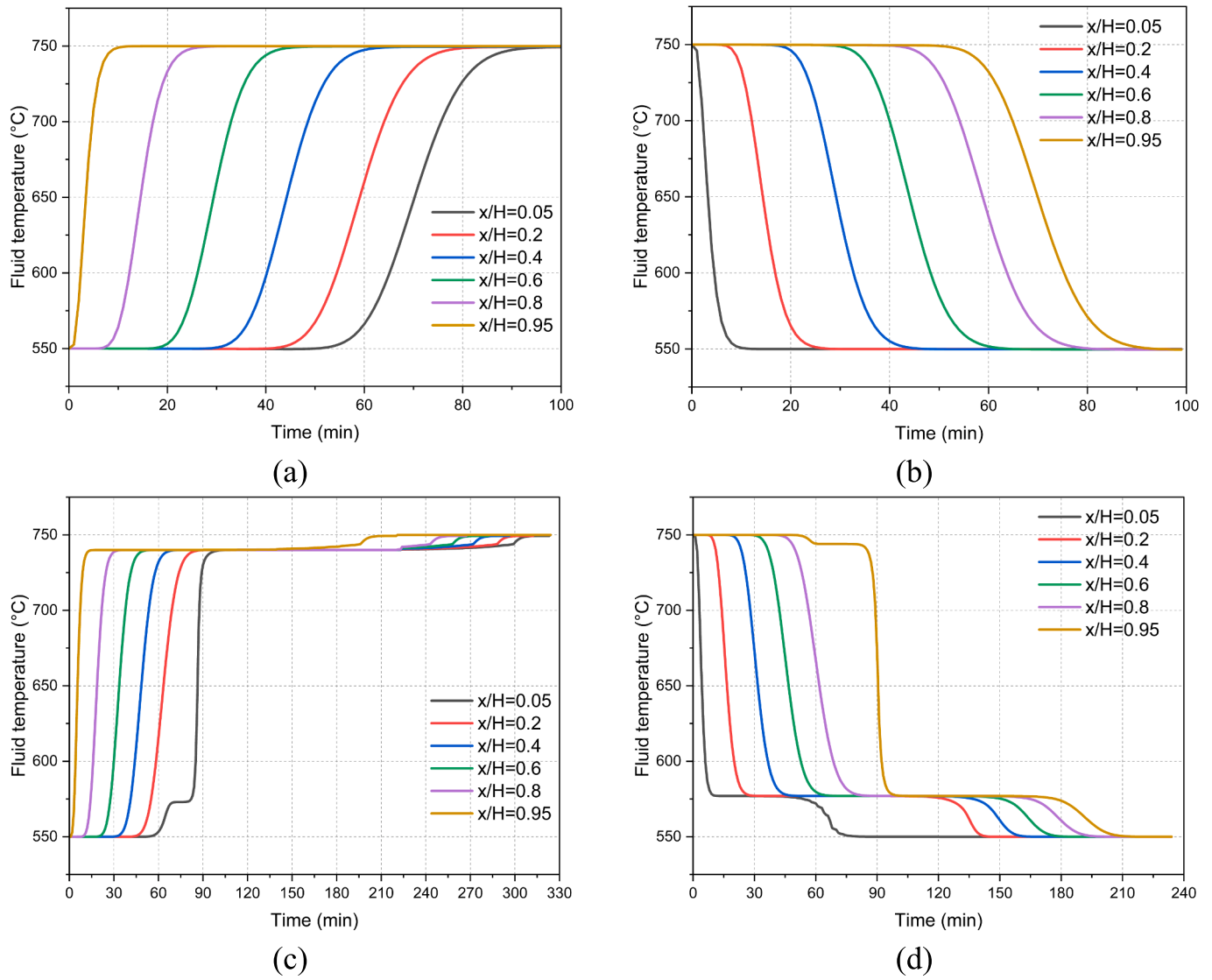
Fig. 6. Comparison of fluid temperature profiles in PBTES systems (porosity = 0.4) for sensible-only and hybrid configurations: (a) charging and (b) discharging for the fully sensible configuration; (c) charging and (d) discharging for the hybrid configuration with $\zeta_1 = \zeta_2 = 10$ %.
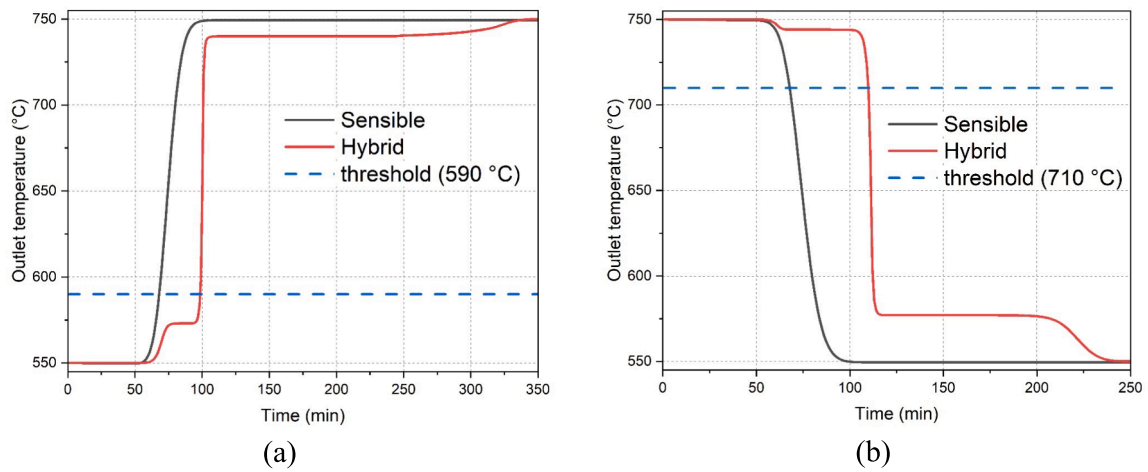

Fig. 7. Comparison of outlet fluid temperature for two configurations: fully sensible (black line) and hybrid with $\zeta_1 = \zeta_2 = 10$ % (red line) during (a) charging and (b) discharging processes, with porosity = 0.4. (For interpretation of the references to color in this figure legend, the reader is referred to the web version of this article.)
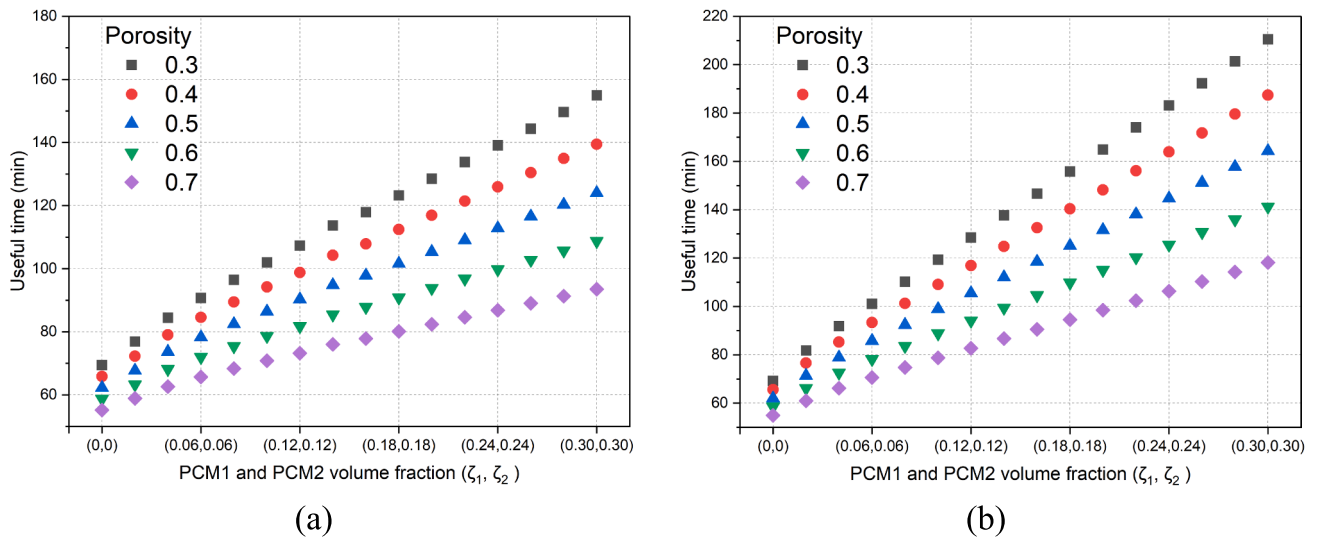
Fig. 8. Useful time during which the outlet fluid temperature remains within the desirable range for (a) charging and (b) discharging processes, across a range of porosity and PCM volume fraction values for hybrid PBTES systems.
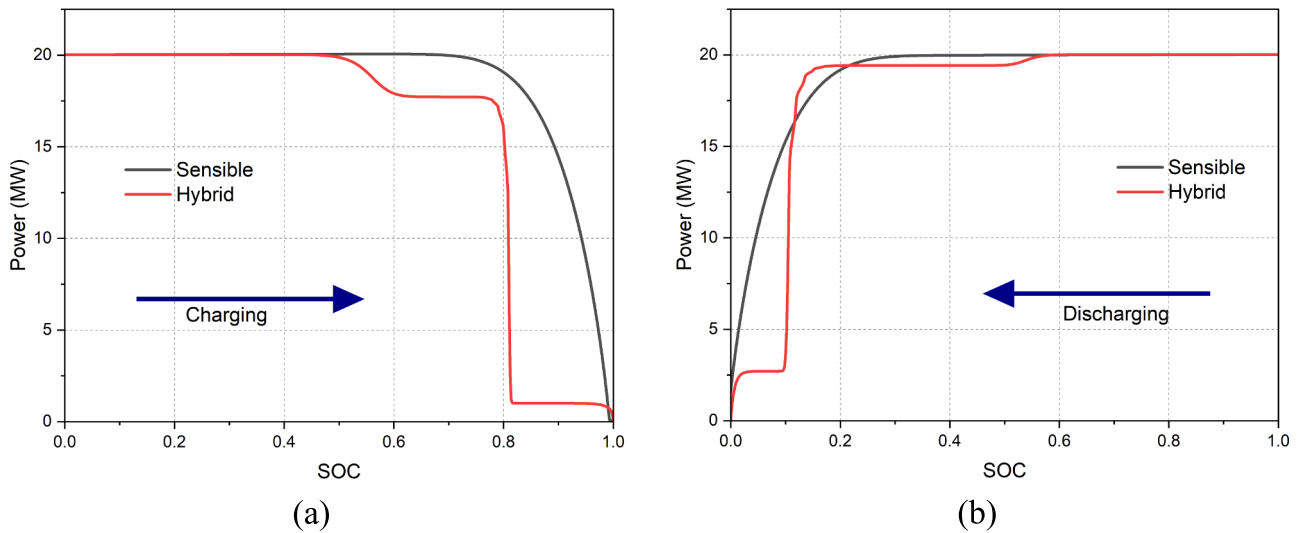
Fig. 9. Comparison of the fully sensible configuration (black line) and the hybrid configuration (red line) with $\zeta_1 = \zeta_2 = 10$ %, showing thermal power versus SOC during (a) charging and (b) discharging processes. (For interpretation of the references to color in this figure legend, the reader is referred to the web version of this article.)

the progression of each process in time. It is important to note that both Fig. 9 and Fig. 10 are presented in the energy dimension rather than the time domain, and therefore, time is not explicitly displayed in the figures. Additionally, these figures are plotted based on the respective SOC for each configuration, considering that the total stored and released energy differs significantly between the configurations. This distinction ensures that the SOC is appropriately contextualized for the energy characteristics of each configuration.

By comparing the liquid fraction contours during charging and discharging processes, several key observations can be made. First, the PCM layer closest to the HTF inlet undergoes phase change earlier than the layer farther downstream. Additionally, a sequential phase change is observed among PCM capsules of the same type, as expected. However, this sequence is not strictly maintained between PCM1 and PCM2 layers, as phase change in one layer may not necessarily complete before the beginning of phase change in the other PCM layer.

During discharge (Fig. 10 (b)) for instance, while it is generally expected that the closer PCM layer (PCM1) solidifies before the farther

PCM2 layer, the last portion of PCM1 ($x/H = 0.09$) begins solidification at a later stage. Meanwhile, the first layer of PCM2 ($x/H = 0.91$) starts to solidify earlier than that of PCM1 ($x/H = 0.09$) due to the significantly higher temperature gradient between the melting point of PCM2 and the surrounding HTF flow. This behavior is particularly noticeable around a SOC value of approximately 0.5. At this stage, a significant portion of the sensible storage medium has discharged to much lower temperatures compared to its initial state at the beginning of the discharge process, as evident in Fig. 6 (d).

Second, the low heat transfer rate during PCM2 layer melting is apparent (in Fig. 10 (a)), primarily due to the lower temperature gradient driving the process. This is reflected in the significantly longer time required for the first PCM2 layer ($x/H = 0.99$) to melt, compared to the observed solidification rate of the first PCM1 layer during discharging. Consequently, the phase change of PCM2 is delayed to a much later stage in the charging process compared to the phase change of PCM1 during discharge. It was also found, based on analysis not presented in this article, that this delay becomes more pronounced as ζ_2
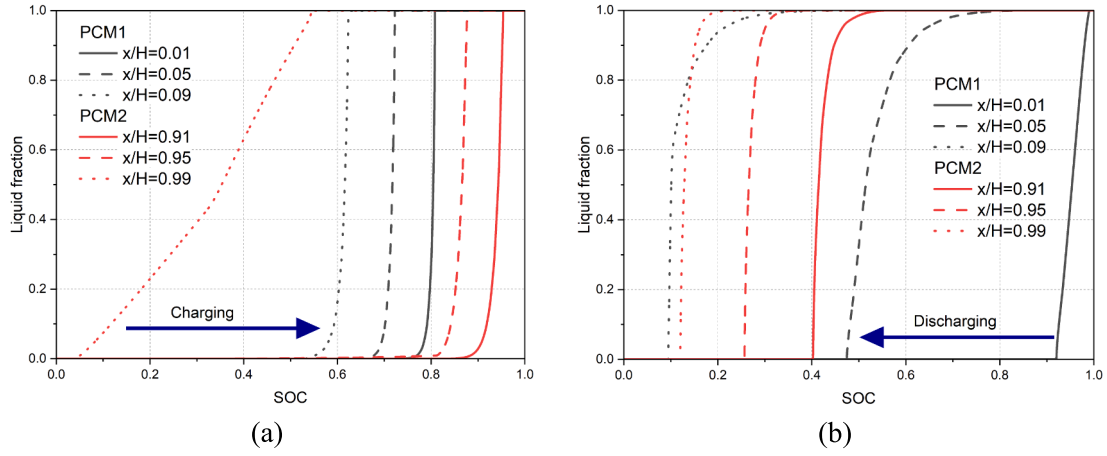
Fig. 10. Liquid fraction at various locations within the PCM1 and PCM2 layers in a hybrid configuration ($\zeta_1 = \zeta_2 = 10$ %) during (a) charging and (b) discharging processes.
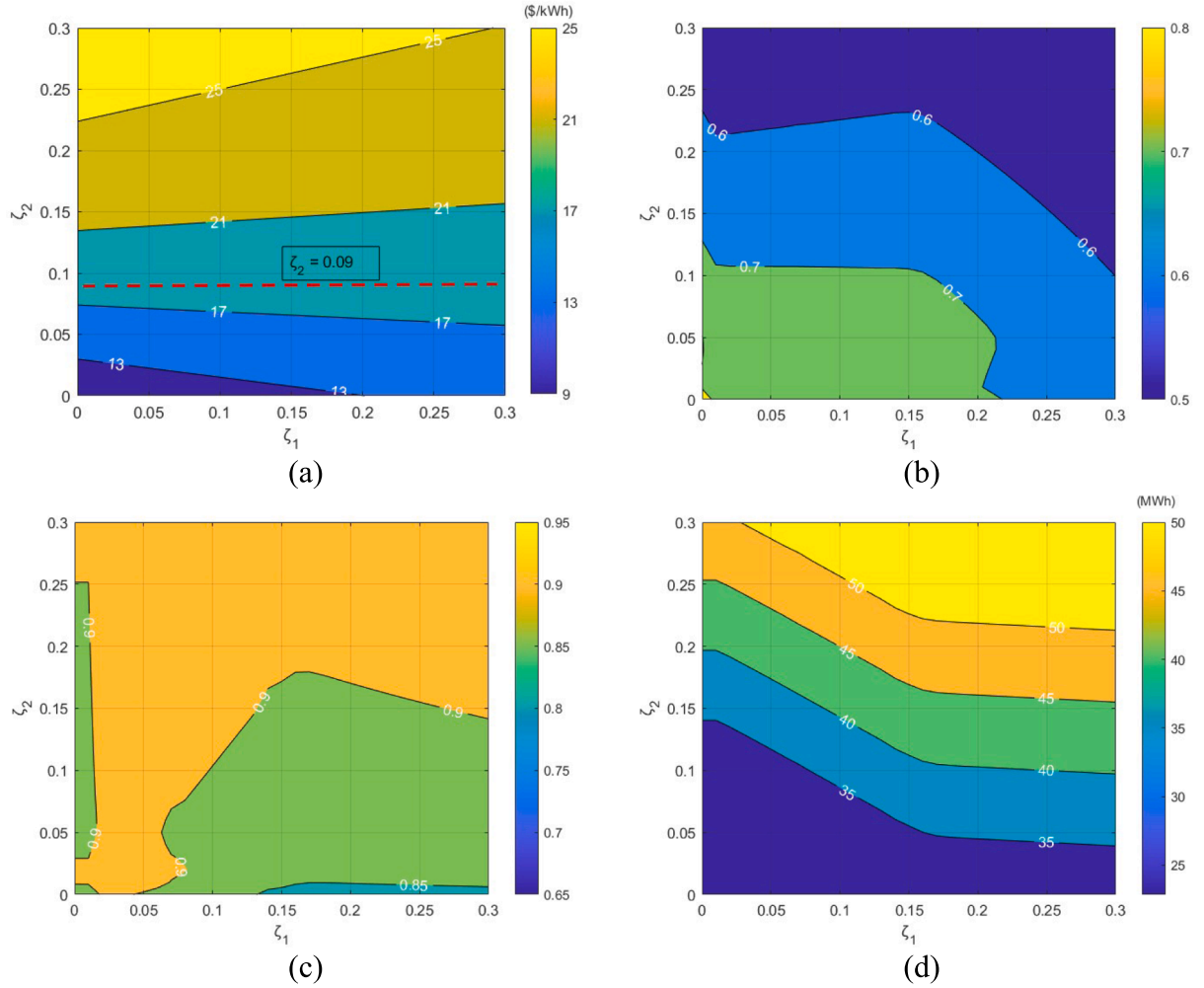

Fig. 11. Parametric study contours for PCM volume fractions ranging from $\zeta_1=\zeta_2=0$ to $\zeta_1=\zeta_2=0.3$, with a porosity of 0.5, illustrating selected KPIs: (a) material cost (b) efficiency (c) average utilization ratio and (d) total released energy.

values increase, leading to a substantially extended charging duration.

Third, simultaneous phase change of portions of PCM1 and PCM2 can occur as observed in Fig. 10 (b) during the discharging process within the SOC range of 0.1 to 0.2. This behavior arises from differing heat transfer dynamics, primarily influenced by the distinct melting temperatures of the two PCM types.

5.5. Parametric study and optimal configurations

To gain a comprehensive understanding of the performance of the

PBTES system, a parametric study was conducted. This section examines the effects of PBTES configurations on KPIs, including efficiency, cost, utilization ratio, and discharged energy. Specifically, the study evaluates the influence of independently varying the volume fractions of PCM1 (ζ_1) and PCM2 (ζ_2) from 0 to 0.3 in increments of 0.01. The resulting KPIs are presented in Fig. 11, offering insights into the relationship between PCM volume fractions and storage performance.

Fig. 11 (a) shows that the material cost of the storage system ranges between approximately 9 and 27 \$/kWh, as calculated using Eq. (8). The lowest cost is observed in the fully sensible configuration, while the cost increases with higher values of ζ_1 and ζ_2. Despite their higher energy density, the increased cost is attributed to the higher material cost of PCMs, as well as additional expenses associated with encapsulation material and fabrication. Generally, the rate of cost increase with ζ_2 (PCM2) is significantly higher than with ζ_1 (PCM1). This is primarily due to PCM2 material cost being approximately four times higher and its greater density, as detailed in Table 1. The red dashed line at $\zeta_2 = 0.09$ represents an intermediate configuration, indicating a potential balance between cost and performance. Along this line, the cost associated with PCM1 might be increasing linearly with storage capacity, resulting in an almost constant total cost as ζ_1 increases.

As shown in Fig. 11 (b), the efficiency of the storage system decreases with the addition of either PCM1 or PCM2 due to the extended charge durations. In fact, PCM2 has a more noticeable impact. This is primarily attributed to the slower heat transfer rate between the HTF and PCM2 during the charging process, a phenomenon discussed in detail in section 5.4 and further explored in the sensitivity study presented in section 5.6. This efficiency behavior is directly associated with the temperature difference between the melting temperature of PCM2 and the charging inlet temperature of the HTF, which therefore offers possibilities for improvements by changing the PCM. The reported efficiency values range from approximately 0.5 to 0.8, reflecting the trade-offs introduced by the incorporation of PCMs into the PBTES.

During charging, it was found (based on analysis not presented in this article), that the utilization ratio generally increases with the addition of PCM1, while PCM2 results in an opposite effect. The highest utilization ratios are observed in configurations with high ζ_1 and low ζ_2, reflecting the improved energy storage within the desirable temperature range as the thickness of the PCM1 layer increases. In contrast, during the discharge cycle, the addition of PCM2 improves the utilization ratio, while PCM1 has a negative impact. The improved performance with increasing ζ_2 is attributed to the heat discharged from PCM2, which has a melting point within the desirable temperature range of the discharge process. To account for the combined effects, the average utilization

ratio across both charging and discharging is plotted in Fig. 11 (c). The results generally indicate that ζ_2 has a smaller negative impact on the utilization ratio compared to ζ_1 on average. Furthermore, at higher values, the combination of ζ_2 and ζ_1 yields high utilization ratios. However, no clear trend emerges due to the opposing effects of PCM1 and PCM2 during the charging and discharging processes.

This observation highlights a practical consideration: depending on the specific application or priority, it may not always be advantageous to include two types of PCMs with different melting points, as done in this study. For instance, if the PBTES is intended to stabilize the outlet HTF temperature during charging, it would be more effective to include only the PCM1 layer. Similarly, only the PCM2 layer should be incorporated for applications benefiting from stabilization during discharging. Including both PCM layers in a process that primarily benefits from one type of PCM can unnecessarily prolong the process duration, as discussed in section 5.3, and result in a lower heat utilization ratio, thereby reducing the overall performance of the storage system.

Fig. 11 (d) presents the total energy released from the PBTES system. Since the simulations terminate once the TES is fully charged or discharged, the total stored and released energy are nearly identical, with only marginal differences due to heat losses to the surroundings. Therefore, only the total discharged energy is reported. The results reveal a clear trend of increasing discharged energy with higher PCM volume fractions, particularly with increasing ζ_2, which is attributed to the higher heat content of PCM2 compared to PCM1. Configurations with low PCM fractions exhibit significantly lower discharged energy, as these are dominated by the sensible storage medium, which has a comparatively limited energy density, as illustrated in Fig. 4. These findings highlight the advantage of PCM integration in enhancing the energy capacity of the system.

From the previous discussion, it is evident that incorporating PCM layers in the PBTES system presents trade-offs. While PCM integration negatively impacts cost and efficiency, it offers significant advantages in terms of energy density, utilization ratio, outlet HTF temperature stability, and total stored and released energy.

To better understand these trade-offs, a Pareto front is plotted in Fig. 12. This plot is derived from the results of the parametric study and considers four key objectives: efficiency, cost, average utilization ratio, and total discharged energy. The results reveal clear trade-offs. At the lower end of the Pareto front, configurations with minimal PCM fractions achieve the lowest cost and highest efficiency. These configurations benefit from the dominance of the sensible storage medium, which is cost-effective and facilitates efficient heat transfer. However, they offer lower discharged energy.
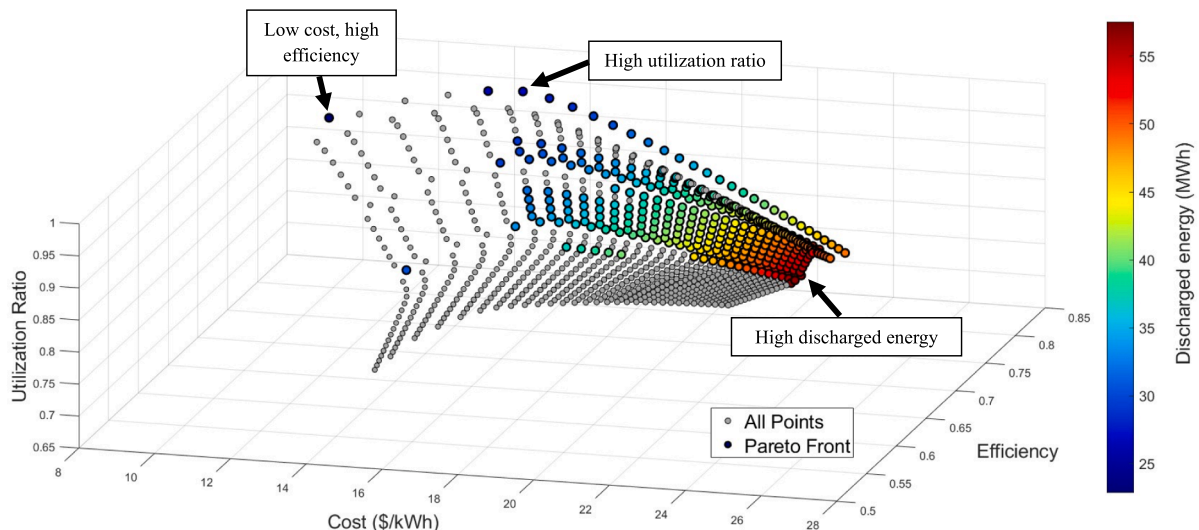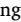

Fig. 12. 3D Pareto front visualization of 4 objectives: cost, utilization ratio, efficiency, and discharged energy.

Table 4

Summary of representative PBTES configurations highlighting key performance trade-offs. Color indicators emphasize favorable (green ▨), moderate (orange ▨), and less favorable (red ▨) values.

Configuration	ζ_1	ζ_2	Cost ($/kWh)	Efficiency	Utilization Ratio	Discharged Energy (MWh)
Lowest Cost	0 %	0 %	9.48 ▨	0.82 ▨	0.91 ▨	22.85 ▨
Balanced Performance (Mid-Pareto)	10 %	10 %	18.89 ▨	0.74 ▨	0.9 ▨	36.22 ▨
Highest Energy Output	30 %	30 %	24.95 ▨	0.51 ▨	0.93 ▨	57.52 ▨

As PCM fractions increase, discharged energy and utilization ratio improve significantly. The highest utilization ratio is observed in the middle of the Pareto front, where PCM integration strikes a balance between energy density and thermal performance. However, this improvement comes with higher costs and a slight reduction in efficiency, reflecting the slower heat transfer rates associated with PCMs. At the upper end of the Pareto front, configurations achieve the highest discharged energy, exceeding 50 MWh. These configurations rely on

high PCM fractions, particularly PCM2, which contribute to the increased energy storage capacity. However, this comes at the expense of higher costs and a more noticeable drop in efficiency, underscoring the trade-off between maximizing energy output and controlling costs.

Fig. 12 presents the Pareto front, highlighting the complex trade-offs between competing objectives in system design. To provide a more comprehensive visualization, a video showcasing the 3D Pareto front from different viewpoints is included in Appendix A. Configurations
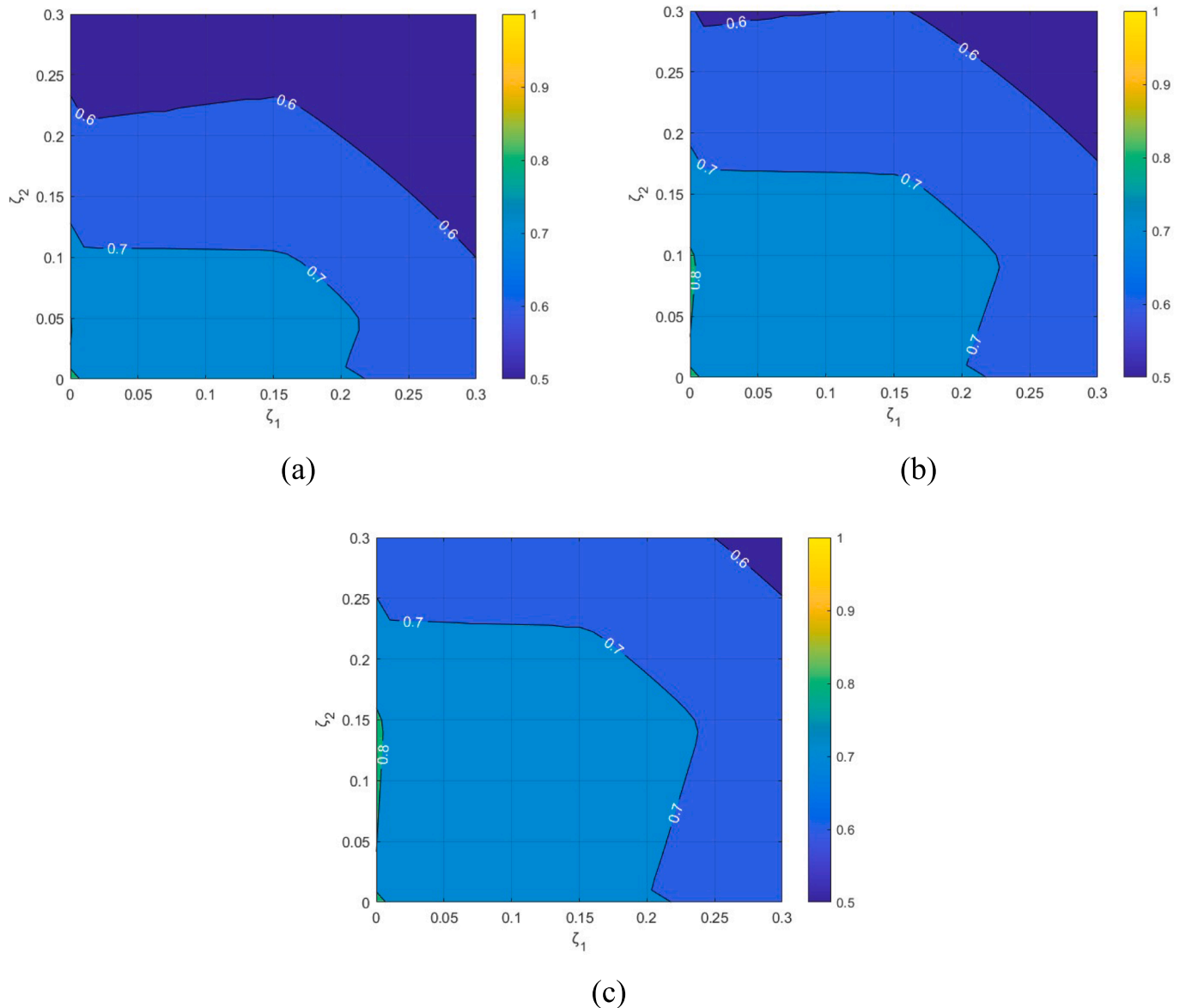

(a)

(b)

(c)

Fig. 13. Efficiency of the PBTES system under different ΔT values between the inlet fluid temperature during charging and the melting temperature of PCM2: (a) $\Delta T = 8$ K, (b) $\Delta T = 18$ K, and (c) $\Delta T = 28$ K.

Table 5

Cost analysis assumptions considered for the payback period evaluation.

Input	Value	Reference
Electricity price ($/MWh)	132.2	[91]
CSP power block efficiency	40 %	[19]
Capacity factor	50 % (2021), 60 % (2030)	[92]

along the Pareto front offer valuable insights into how design choices influence cost, efficiency, utilization ratio, and energy output, facilitating informed decision-making for tailored energy storage solutions. Given the multifaceted nature of this problem, decision-makers may prioritize certain objectives over others, leading to different optimized hybrid configurations. These priorities will vary depending on the perspective and goals of stakeholders, such as engineers, researchers, financiers, or policy makers, each of whom may emphasize specific aspects of the system's performance or feasibility.

To complement the graphical analysis, Table 4 presents a detailed quantitative summary of three representative PBTES configurations selected from the Pareto front, each illustrating distinct performance trade-offs. The table highlights how varying the PCM volume fractions (ζ_1 and ζ_2) influences KPIs. The "Lowest Cost" configuration, with no PCM layers, achieves the most favorable cost and efficiency values but results in the lowest discharged energy. Conversely, the "Highest Energy Output" configuration, with maximum PCM integration, delivers the highest stored energy and utilization ratio, though with increased cost and reduced efficiency. The "Balanced Performance" configuration offers a middle ground, providing moderate cost and efficiency while maintaining high utilization and energy output. This summary provides practical insights into how PCM integration affects both technical and economic aspects of PBTES systems, aiding decision-makers in selecting optimal configurations based on specific application needs.

In practice, the interpretation of trade-offs depends heavily on specific project goals and constraints. For example, when retrofitting an existing sensible PBTES system to boost storage capacity and improve outlet fluid temperature stability, replacing part of the sensible storage medium with PCM capsules in a balanced configuration (e.g., $\zeta_1 = \zeta_2 = 10$ %) can be highly effective. This approach significantly increases energy density (by more than 50 %) with a relatively modest investment, avoiding the need for costly system modifications such as additional tanks, auxiliary components, or piping adjustments. On the other hand, for new projects aiming to support intermittent renewable sources, where extended discharge duration is a priority, a configuration with higher PCM fractions ($\zeta_1 = \zeta_2 = 30$ %) may be preferable, as it maximizes discharged energy despite higher costs and lower efficiency, suitable for applications requiring long-duration, stable thermal output.

5.6. Influence of temperature difference between HTF inlet temperature and PCM2 melting point

The slow melting rate of PCM2, caused by the relatively low tem-

the base case shown in Fig. 13 (a), PCM2 has a melting point of 742 °C, while in Fig. 13 (b) and Fig. 13 (c), the melting temperature is reduced to 732 °C and 722 °C, respectively.

The results of the sensitivity analysis reported in Fig. 13 demonstrate the significant influence of ΔT on the efficiency of PBTES systems. At low ΔT, PCM2's inefficient melting behavior notably reduces efficiency, especially at higher ζ_2 values. Increasing ΔT to 18 K and 28 K improves heat transfer and accelerates the phase change process, resulting in generally higher efficiencies.

While increasing ΔT improves PCM2 melting and enhances overall efficiency, excessively high ΔT can introduce drawbacks. Fig. 13 (c) proves that a higher ΔT, achieved by lowering the melting point of PCM2 for the same inlet temperature, directly impacts the temperature at which the outlet fluid remains stable. This stability may be critical for applications requiring consistent thermal performance at specific temperatures. A reduction in outlet stability can compromise the TES system's ability to meet the thermal requirements of downstream processes. Therefore, it is crucial to carefully balance ΔT to optimize PCM2 melting while ensuring stable and reliable outlet fluid temperatures for effective system performance.

5.7. Cost analysis

To better understand the cost dynamics of PBTES systems, two types of cost analysis are conducted: a simple payback period analysis and material cost sensitivity analysis.

5.7.1. Payback period

The simple payback period method provides a preliminary rough estimate of the time required to recover the additional investment associated with integrating PCMs into the PBTES system. This analysis translates the enhanced thermal performance, resulting from increased storage capacity due to PCM integration, into monetary value by considering key economic and operational parameters, including electricity price, power block efficiency, and plant capacity factor, as summarized in Table 5.

The total PCM investment cost accounts for the material expense of replacing a specific amount of the sensible storage medium with encapsulated PCMs, as studied in this work. This cost is calculated using Eq. (25), which is a modified form of the general cost equation (Eq. (8)), specifically adjusted to reflect the additional investment required for PCM integration:

$$PCM\ investment\ cost\ (\$) =$$
$$\sum_{j=1}^{2} V^* \zeta_{PCM_j} (1 - \varepsilon) \left(\rho_p M_p + \psi_{enc} \left(M_{fab} + \rho_{enc} M_{enc} \right) \right) \qquad (25)$$

The annual energy benefits represent the additional revenue generated due to the improved thermal performance of the system and are calculated as:

$$Annual\ energy\ benefits\ (\$/year) =$$
$$Increased\ storage\ capacity\ (MWh)^* Electricity\ price\ (\$/MWh)^* Power\ block\ efficiency^* Capacity\ factor^* 365 \qquad (26)$$

perature difference (ΔT) between the inlet HTF temperature during charging and PCM2's melting point, leads to a prolonged charging cycle and reduced system efficiency. This issue has been discussed in terms of the liquid fraction in section 5.4 and HTF temperature profiles in sections 5.2 and 5.3. To address this issue, a sensitivity analysis was performed to evaluate the impact of ΔT on TES efficiency by keeping the inlet fluid temperature as is and lowering the melting point of PCM2. In

Equation (26) estimates the annual energy benefits ($/year) resulting from PCM integration by translating the additional storage capacity into economic value. The increased capacity, measured in MWh, reflects the extra thermal energy stored due to PCM use. This energy is converted to electricity based on the power block efficiency, while the capacity factor accounts for the system's operational availability. The electricity price determines the financial value of the generated electricity, and the full
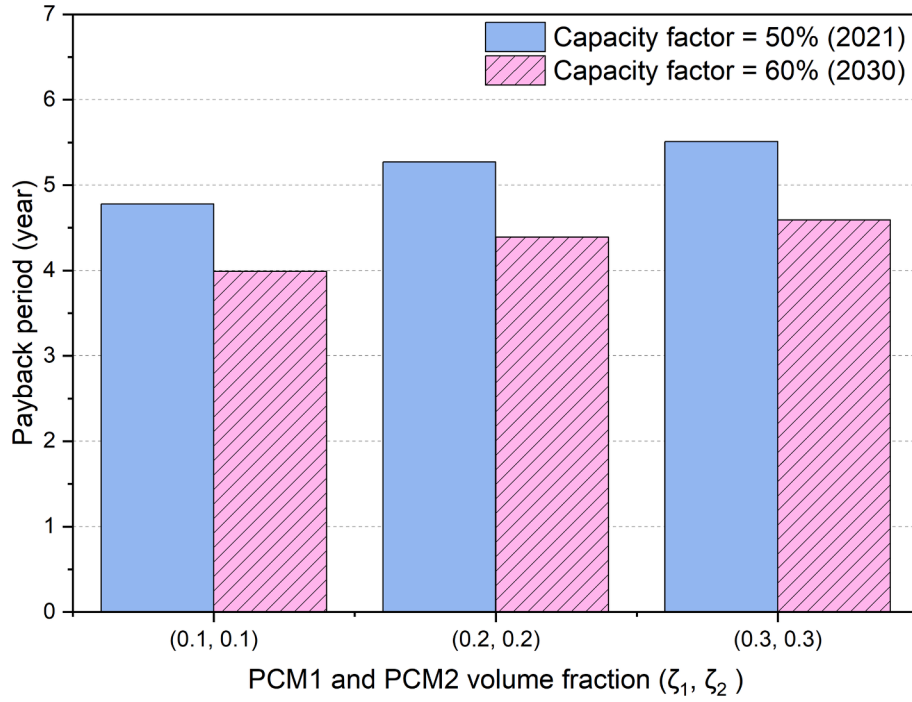
Fig. 14. Simple payback period for partial replacement of sensible filler with PCMs in PBTES.

year operation is considered by factoring the estimate over 365 days. This provides a clear measure of the yearly revenue improvement driven by enhanced thermal performance.

The simple payback period, which relates the PCM investment cost to the annual energy benefits, is then calculated using:

$$Payback\ period\ (year) = \frac{PCM\ investment\ cost\ (\$)}{Annual\ energy\ benefits(\$/year)} \quad (27)$$

Given the case-dependent nature of the payback period, example scenarios are evaluated with PCM volume fractions $\zeta_1 = \zeta_2 = 10\ \%$, $20\ \%$, and $30\ \%$. These configurations yield 58 %, 105 %, and 152 % increases in storage capacity, respectively, compared to the fully sensible storage baseline, as shown in Fig. 4. The economic evaluation is based on the assumptions listed in Table 5.

The payback period analysis presented in Fig. 14 illustrates the combined impact of PCM volume fraction and plant capacity factor on the economic viability of PCM integration in PBTES systems. As the PCM volume fraction increases from 10 % to 30 %, the payback period also rises, reflecting the higher initial investment required for greater PCM content, despite the corresponding increase in storage capacity. Under the current global weighted average CSP capacity factor of 50 %, representative of 2021, payback periods range from approximately 4.8 to 5.5 years, indicating reduced economic returns at higher PCM volumes in present-day operating conditions. However, Khan et al. [92] report that with ongoing advancements in TES, power block flexibility, and solar field performance, capacity factors for new CSP plants are expected to reach 60 % by 2030. Under this improved operational scenario, the payback period is significantly reduced, falling between 4.0 and 4.7 years across all PCM configurations. This demonstrates the critical role of plant utilization in improving the financial justification
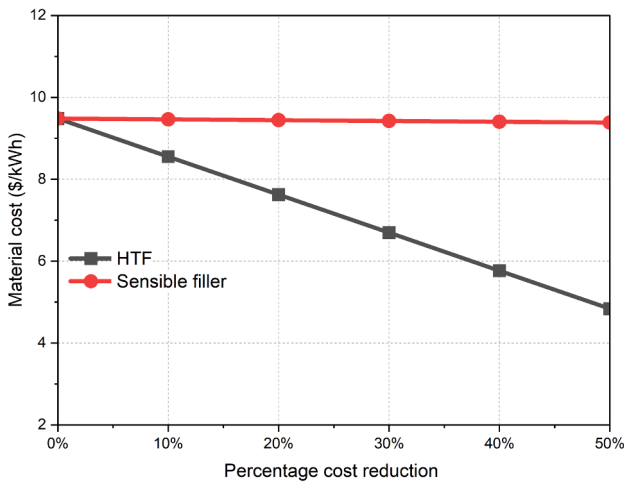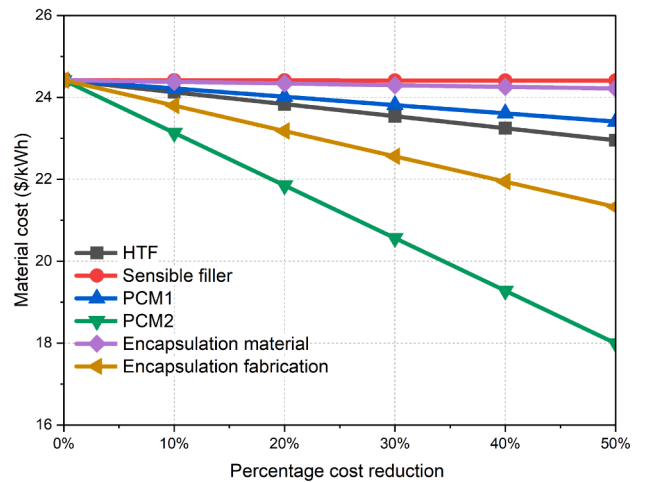
Fig. 15. Material cost sensitivity of PBTES under component cost reductions for (a) sensible configuration and (b) hybrid configuration with $\zeta_1 = \zeta_2 = 30\ \%$.

for PCM integration. Even at higher PCM volume fractions, enhanced system performance under future conditions helps offset the increased investment, making larger PCM deployments more economically viable.

5.7.2. Sensitivity analysis

To extend the economic evaluation of the studied PBTES, sensitivity analysis is conducted by progressively reducing the material costs of each component by up to 50 %. The two extreme cases studied in this work are analyzed to explore how variations in material prices influence the overall storage material cost, providing insight into cost optimization opportunities for both sensible and hybrid PBTES configurations.

Fig. 15 (a) presents the material cost sensitivity of a fully sensible PBTES configuration. While Fig. 4 shows that the sensible storage medium stores the majority of the system's heat in a fully sensible configuration, reducing its cost by 50 % yields less than a 1 % reduction in total storage cost. In contrast, the HTF cost has a much greater impact, with a 50 % reduction in HTF cost lowering the total material cost from approximately 9.5 $/kWh to about 4.8 $/kWh. This highlights the dominant role of sodium HTF pricing in influencing the economic viability of the studied sensible-only storage systems. Such insight suggests that while sodium offers technical advantages in terms of thermal performance, its high cost poses a significant economic drawback, driving future research directions towards identifying alternative HTFs or system designs that maintain performance while reducing cost.

In contrast, the hybrid PBTES configuration ($\zeta_1 = \zeta_2 = 30$ %) introduces several additional cost components, including the costs of PCM1, PCM2, encapsulation material, and encapsulation fabrication. Among these, PCM2 and encapsulation fabrication costs were found to have the most significant effect, as depicted in Fig. 15 (b). A 50 % reduction in PCM2 cost led to a substantial decrease in overall material cost by up to 25 %, while a similar reduction in encapsulation fabrication cost alone resulted in a 13 % decrease. Additionally, reducing the costs of HTF and PCM1 by 50 % led to a moderate decline of about 5 % in the total material cost. In comparison, cost reductions for the sensible filler and encapsulation material had a relatively insignificant impact, with overall cost savings of less than 1 %. These findings highlight the significant influence of PCM2 and encapsulation fabrication costs, emphasizing their importance in determining the cost-effectiveness of hybrid PBTES configurations.

It should be noted that this section provides a general overview of the potential economic benefits of retrofitting sensible PBTES systems, based on simplified calculations. When increased energy storage capacity is needed, conventional solutions often require substantial investments in larger storage tanks, additional filler material, greater volumes of HTF, and extended piping networks. In contrast, replacing the existing sensible filler with encapsulated PCMs presents a more cost-effective alternative, making such retrofitting even more economically attractive under these circumstances.

5.8. Overview of hybrid TES concepts

Several hybrid TES systems, combining sensible and latent heat storage, have been developed to enhance energy density and system flexibility across a range of temperature-dependent applications. A summary of various hybrid TES concepts across a range of applications is presented in Table 6.

In low-temperature applications (40–80 °C), such as domestic hot water systems, water-based TES integrated with PCMs can boost storage capacity by up to 66.7 % [93]. Medium-temperature systems (110–150 °C), used in district heating and industrial waste heat recovery, often pair thermal oils with PCMs, achieving storage gains of up to 88.5 % [94]. In higher temperature range applications (160–220 °C), especially industrial steam systems, hybrid TES integrates steam storage with salt-based PCMs, enhancing energy density by up to 121 % [95]. Lastly, hybrid TES systems demonstrate their effectiveness even under extreme conditions; cryogenic TES, applied in liquid air energy storage within a temperature range of −168 to 30 °C, combines quartz with cryogenic PCMs and achieves efficiency improvements exceeding 10 % [96].

The scalability and practicality of hybrid TES systems depend on application-specific design and material considerations. Low-temperature systems are highly practical and easy to integrate but are best suited for small-scale use. Medium-temperature systems offer better scalability for industrial settings, though their complexity can limit ease of deployment. High-temperature hybrid TES solutions provide a practical option for retrofitting existing industrial systems, with moderate scalability depending on design constraints. Cryogenic systems, while scalable for large-scale storage, face significant practical challenges due to the technical demands of low-temperature PCM handling. Overall, hybrid TES concepts show strong potential for industrial scalability when carefully designed to balance performance with material and operational complexities.

The hybrid PBTES system studied in this work offers a practical and scalable solution within the high-temperature range (>500 °C), comparable to other hybrid TES configurations. By selectively replacing portions of the sensible filler material with encapsulated PCMs, the hybrid PBTES achieves significant enhancements in storage capacity, compared to fully sensible designs, while maintaining a relatively simple structure conducive to retrofitting. Unlike more complex shell-and-tube, the hybrid PBTES leverages the inherent advantages of packed bed systems, such as modularity and cost-effectiveness. These attributes, combined with the demonstrated improvements in energy density and thermal stability, highlight the practical viability of the PBTES system for high-temperature TES in medium- to large-scale CSP applications.

6. Conclusions

This study conducts a comprehensive numerical investigation into hybridizing sensible-based packed bed thermal energy storage (PBTES) by incorporating two types of encapsulated metallic-based phase change

Table 6
Overview of different hybrid TES concepts.

TES concept	Application	Materials	Temperature range	Practicality and scalability	Remarks	Reference
Steam storage with external PCM modules	Industrial retrofit	Water/steam (HTF + sensible), NaNO$_3$–LiNO$_3$ (PCM)	160 to 220 °C	High practicality; moderate scalability	121 % increase in energy density	[95]
Inverted shell-and-tube HX	District/process heating, waste heat recovery	Marlotherm SH (HTF + sensible), HDPE (PCM)	110 to 150 °C	Medium practicality; good scalability	88.5 % storage capacity increase	[94]
Water tank with PCM module	Solar domestic hot water	Water (HTF + sensible), sodium acetate trihydrate + graphite (PCM)	40 to 80 °C	High practicality; low scalability	Up to 67 % capacity increase with PCM modules	[93]
Integrated sensible-latent TES for LAES	Liquid air energy storage (LAES)	Quartz (sensible), BCES-Cryo-4 (PCM), thermal oil (HTF)	−168 to 30 °C	Medium practicality; scalable	>10 % efficiency improvement	[96]

materials (PCMs), each positioned at opposite ends of the storage tank. This work presents the first systematic investigation of metallic-based PCMs in a multi-layered hybrid PBTES system, particularly regarding their unique capability to substantially improve storage density and thermal stability throughout charging and discharging processes. Improved temperature stability positively affects the power block output and efficiency and hence it is a key design parameter for TES in power production applications. This approach explores the potential performance enhancement of next-generation high-temperature concentrated solar power applications. The hybrid configuration leverages the latent heat of fusion and the near-isothermal phase change behavior of PCMs. The PCMs were carefully selected to have appropriate melting temperatures. A validated concentric dispersion model was used to simulate a wide range of configurations with each PCM layer thickness varying from 0 to 30 %, for a given TES volume. Based on the results, the key findings can be classified concerning thermal performance, trade-offs and economic viability, as follows:

Thermal performance:

- Incorporating PCMs into the PBTES significantly increases storage capacity, achieving up to a 250 % improvement in energy density compared to the fully sensible configuration, particularly at low porosity levels where higher particle density amplifies PCM contributions.
- The hybrid configuration extends charging and discharging times while stabilizing HTF temperature plateaus at 742 °C and 575 °C, corresponding to the melting points of PCM2 and PCM1, respectively, demonstrating enhanced thermal stability and energy storage performance.
- PCM integration enhances outlet fluid temperature stability, increasing the duration within the desirable temperature range by up to 220 % during charging and 300 % during discharging, emphasizing the importance of PCM volume fractions in improving thermal performance.
- The hybrid configuration exhibits distinct thermal power behavior, with stabilization phases linked to PCM1 and PCM2 phase changes and broader SOC ranges during discharging, highlighting the critical role of PCM layer dynamics.

Trade-offs:

- Efficiency and utilization ratio are strongly influenced by PCM selection and distribution, with PCM1 enhancing charging performance and PCM2 improving discharging performance, underscoring the need for tailored designs based on specific operational requirements.
- While PCM integration enhances energy density, utilization ratio, and discharged energy, it increases costs and reduces efficiency, necessitating careful optimization to balance application priorities.
- Adjusting the temperature difference (ΔT) between the inlet HTF and PCM2′s melting point improves PCM2 melting and system efficiency. However, excessive ΔT compromises outlet temperature stability, highlighting the need for a balanced approach.

Economic viability:

- PCM integration in PBTES is economically viable, with payback periods of 4.8–5.5 years at 50 % CSP capacity factor, reduced to 4.0–4.7 years at 60 %.
- Cost sensitivity analysis reveals that reducing PCM2 and encapsulation fabrication costs by 50 % lowers total material costs by up to 25 % and 13 %, respectively, further enhancing the cost-effectiveness of hybrid PBTES systems.

In conclusion, hybridizing sensible-based PBTES with PCMs has significant potential to enhance storage capacity, thermal stability, and

energy efficiency for high-temperature applications. By optimizing PCM selection, configuration, and operating conditions, the trade-offs between cost, efficiency, and performance can be effectively managed to tailor the system for specific applications. Given the modularity, material availability, and design simplicity of the proposed hybrid design, the system holds strong potential for industrial-scale deployment in next-generation CSP plants and other high-temperature process heat applications.

While this work is limited to studying the influence of metallic PCMs on the performance of PBTES, future research directions might include a comparison of metallic and salt PCMs to better understand the advantages and limitations of each in thermal storage applications. Additionally, investigating the long-term cycling behavior and thermal degradation of the considered Cu-Mg-Si PCM is essential to evaluate its durability under repeated melting-solidification cycles. Furthermore, system-level techno-economic and life-cycle assessments of the hybrid PBTES configuration would further inform optimal material selection for specific applications.

Use of artificial intelligence (AI) statement

OpenAI language model (ChatGPT 4o) was used in this work. The AI contributions were limited to language editing and improving clarity of the text. After using this tool-service, the authors reviewed and edited the content as needed and took full responsibility for the publication's content.

CRediT authorship contribution statement

Asem Alemam: Writing – original draft, Visualization, Validation, Software, Investigation, Formal analysis, Conceptualization. **Saman Nimali Gunasekara:** Writing – review & editing, Methodology. **Justin NingWei Chiu:** Writing – review & editing, Supervision, Resources. **Klarissa Niedermeier:** Writing – review & editing, Methodology. **Imran Afgan:** Writing – review & editing, Supervision.

Declaration of competing interest

The authors declare that they have no known competing financial interests or personal relationships that could have appeared to influence the work reported in this paper.

Acknowledgements

Appendix A. Supplementary data

Supplementary data to this article can be found online at https://doi.org/10.1016/j.applthermaleng.2025.127375.

Data availability

Data will be made available on request.

References

[1] Q. Hou, N. Zhang, E. Du, M. Miao, F. Peng, C. Kang, Probabilistic duck curve in high PV penetration power system: concept, modeling, and empirical analysis in China, Appl. Energy 242 (November 2018) (2019) 205–215, https://doi.org/10.1016/j.apenergy.2019.03.067.

[2] K.M. Kennedy, et al., The role of concentrated solar power with thermal energy storage in least-cost highly reliable electricity systems fully powered by variable

renewable energy, Adv. Appl. Energy 6 (Jun. 2022), https://doi.org/10.1016/j.adapen.2022.100091.

[3] LDES Council and McKinsey & Company. Net-zero power Long duration energy storage for a renewable grid. 2022. [Online]. Available: www.ldescouncil.com.

[4] A. Alemam, M.I. Al-Widyan, Technical, economic, and environmental assessment of integrating solar thermal systems in existing district heating systems under jordanian climatic conditions, J. Sustain. Devel. Energy Water Environ. Syst. 10 (3) (2022), https://doi.org/10.13044/j.sdewes.d9.0395.

[5] R.D. Selvakumar, J. Wu, I. Afgan, Y. Ding, A.K. Alkaabi, Melting performance enhancement in a thermal energy storage unit using active vortex generation by electric field, J. Energy. Storage 67 (Sep. 2023), https://doi.org/10.1016/j.est.2023.107593.

[6] M. Faizan, A. K. Alkaabi, B. Nie, I. Afgan, Thermal energy storage integration with nuclear power: A critical review, Aug. 15, 2024, Elsevier Ltd. doi: 10.1016/j.est.2024.112577.

[7] A. Alemam, V. Eveloy, I. Afgan, Numerical investigation of aluminum-silicon solidification in a novel high temperature latent heat thermal energy storage system, J. Energy Storage 114 (Apr. 2025) 115767, https://doi.org/10.1016/j.est.2025.115767.

[8] S.S. Mostafavi Tehrani, Y. Shoraka, K. Nithyanandam, R.A. Taylor, Shell-and-tube or packed bed thermal energy storage systems integrated with a concentrated solar power: A techno-economic comparison of sensible and latent heat systems, Appl. Energy. 238 (2019) 887–910, https://doi.org/10.1016/j.apenergy.2019.01.119.

[9] A.S. Mohammad, A.A. Khasawneh, A. Hamza, Simulation and optimization of 100 MW central tower CSP power plant, Appl. Solar Energy (2024), https://doi.org/10.3103/S0003701X24602369.

[10] G. Zanganeh, A. Pedretti, A. Haselbacher, A. Steinfeld, Design of packed bed thermal energy storage systems for high-temperature industrial process heat, Appl. Energy 137 (Jan. 2015) 812–822, https://doi.org/10.1016/j.apenergy.2014.07.110.

[11] I. González, C.D. Pérez-Segarra, O. Lehmkuhl, S. Torras, A. Oliva, Thermo-mechanical parametric analysis of packed-bed thermocline energy storage tanks, Appl. Energy 179 (Oct. 2016) 1106–1122, https://doi.org/10.1016/j.apenergy.2016.06.124.

[12] V. M. B. Nunes, C. S. Queirós, M. J. V. Lourenço, F. J. V. Santos, and C. A. Nieto de Castro, "Molten salts as engineering fluids – A review: Part I. Molten alkali nitrates," Dec. 01, 2016, Elsevier Ltd. doi: 10.1016/j.apenergy.2016.09.003.

[13] M. Biencinto, R. Bayón, L. González, R. Christodoulaki, E. Rojas, Integration of a parabolic-trough solar field with solid-solid latent storage in an industrial process with different temperature levels, Appl. Therm. Eng 184 (Feb. 2021), https://doi.org/10.1016/j.applthermaleng.2020.116263.

[14] Solutia Inc., "THERMINOL® VP-1 Vapor Phase / Liquid Phase Heat Transfer Fluid," 1999. Accessed: Aug. 05, 2024. [Online]. Available: www.therminol.com.

[15] R. Ferri, A. Cammi, D. Mazzei, Molten salt mixture properties in RELAP5 code for thermodynamic solar applications, Int. J. Therm. Sci. 47 (12) (Dec. 2008) 1676–1687, https://doi.org/10.1016/j.ijthermalsci.2008.01.007.

[16] F. Müller-Trefzer, K. Niedermeier, M. Daubner, T. Wetzel, Experimental investigations on the design of a dual-media thermal energy storage with liquid metal, Appl. Therm. Eng 213 (Aug. 2022), https://doi.org/10.1016/j.applthermaleng.2022.118619.

[17] K. Niedermeier, J. Flesch, L. Marocco, T. Wetzel, Assessment of thermal energy storage options in a sodium-based CSP plant, Appl. Therm. Eng 107 (Aug. 2016) 386–397, https://doi.org/10.1016/j.applthermaleng.2016.06.152.

[18] P. Li, et al., Thermal and transport properties of NaCl-KCl-ZnCl2 eutectic salts for new generation high-temperature heat-transfer fluids, J. Solar Energy Eng., Trans. ASME 138 (5) (2016) Oct, https://doi.org/10.1115/1.4033793.

[19] K. Niedermeier, L. Marocco, J. Flesch, G. Mohan, J. Coventry, T. Wetzel, Performance of molten sodium vs. molten salts in a packed bed thermal energy storage, Appl. Therm. Eng 141 (Aug. 2018) 368–377, https://doi.org/10.1016/j.applthermaleng.2018.05.080.

[20] S.N. Gunasekara, et al., Thermal energy storage materials (Tesms)—what does it take to make them fly? Crystals (Basel) 11 (11) (2021) Nov, https://doi.org/10.3390/cryst11111276.

[21] V.A. Lebedev, A. Elsayed, A. Amer, V. Lebedev, Thermal energy storage by using latent heat storage materials, Int. J. Sci. Eng. Res. 9 (5) (2018) 1442–1447.

[22] A. Alemam, et al., Experimental demonstration of a dispatchable power-to-power high temperature latent heat storage system, J. Energy. Storage 86 (May 2024) 111241, https://doi.org/10.1016/j.est.2024.111241.

[23] J. Lu, T. Yu, J. Ding, Y. Yuan, Thermal storage performance of molten salt thermocline system with packed phase change bed, Energy. Convers. Manag 102 (Jul. 2015) 267–274, https://doi.org/10.1016/j.enconman.2014.10.049.

[24] X. Yang, Z. Cai, An analysis of a packed bed thermal energy storage system using sensible heat and phase change materials, Int. J. Heat. Mass. Transf 144 (Dec. 2019), https://doi.org/10.1016/j.ijheatmasstransfer.2019.118651.

[25] Q. Mao, Y. Zhang, Thermal energy storage performance of a three-PCM cascade tank in a high-temperature packed bed system, Renew. Energy 152 (Jun. 2020) 110–119, https://doi.org/10.1016/j.renene.2020.01.015.

[26] M.J. Li, B. Jin, J.J. Yan, Z. Ma, M.J. Li, Numerical and Experimental study on the performance of a new two-layered high-temperature packed-bed thermal energy storage system with changed-diameter macro-encapsulation capsule, Appl. Therm. Eng 142 (Sep. 2018) 830–845, https://doi.org/10.1016/j.applthermaleng.2018.07.026.

[27] R. Majumdar, S.K. Saha, Computational study of performance of cascaded multi-layered packed-bed thermal energy storage for high temperature applications, J. Energy. Storage 32 (Dec. 2020), https://doi.org/10.1016/j.est.2020.101930.

[28] K.E. Elfeky, A.G. Mohammed, N. Ahmed, L. Lu, Q. Wang, Thermal and economic evaluation of phase change material volume fraction for thermocline tank used in concentrating solar power plants, Appl. Energy 267 (Jun. 2020), https://doi.org/10.1016/j.apenergy.2020.115054.

[29] M. Wu, C. Xu, Y. He, Cyclic behaviors of the molten-salt packed-bed thermal storage system filled with cascaded phase change material capsules, Appl. Therm. Eng 93 (Jan. 2016) 1061–1073, https://doi.org/10.1016/j.applthermaleng.2015.10.014.

[30] M.E. Zayed, et al., Applications of cascaded phase change materials in solar water collector storage tanks: a review, Sol. Energy Mater. Sol. Cells 199 (Sep. 2019) 24–49, https://doi.org/10.1016/j.solmat.2019.04.018.

[31] H.J. Xu, C.Y. Zhao, Analytical considerations on optimization of cascaded heat transfer process for thermal storage system with principles of thermodynamics, Renew. Energy 132 (Mar. 2019) 826–845, https://doi.org/10.1016/j.renene.2018.07.135.

[32] H.J. Xu, C.Y. Zhao, Thermal performance of cascaded thermal storage with phase-change materials (PCMs). Part I: Steady cases, Int. J. Heat. Mass. Transf 106 (Mar. 2017) 932–944, https://doi.org/10.1016/j.ijheatmasstransfer.2016.10.054.

[33] H.J. Xu, C.Y. Zhao, Thermal performance of cascaded thermal storage with phase-change materials (PCMs). Part II: Unsteady cases, Int. J. Heat. Mass. Transf 106 (Mar. 2017) 945–957, https://doi.org/10.1016/j.ijheatmasstransfer.2016.10.066.

[34] S. Zhang, Y. Li, Y. Yan, Hybrid sensible-latent heat thermal energy storage using natural stones to enhance heat transfer: Energy, exergy, and economic analysis, Energy 286 (Jan. 2024), https://doi.org/10.1016/j.energy.2023.129530.

[35] G. Zanganeh, M. Commerford, A. Haselbacher, A. Pedretti, A. Steinfeld, Stabilization of the outflow temperature of a packed-bed thermal energy storage by combining rocks with phase change materials, Appl. Therm. Eng 70 (1) (Sep. 2014) 316–320, https://doi.org/10.1016/j.applthermaleng.2014.05.020.

[36] G. Zanganeh, R. Khanna, C. Walser, A. Pedretti, A. Haselbacher, A. Steinfeld, Experimental and numerical investigation of combined sensible-latent heat for thermal energy storage at 575°C and above, Sol. Energy 114 (Apr. 2015) 77–90, https://doi.org/10.1016/j.solener.2015.01.022.

[37] K. Niedermeier, S. Sinning, F. Müller-Trefzer, L. Marocco, T. Wetzel, Liquid metal as heat transfer fluid in dual-media sensible and latent heat storage. in 17th UK Heat Transfer Conference (UKHTC2021), Manchester, UK, Apr. 2022.

[38] B.C. Zhao, M.S. Cheng, C. Liu, Z.M. Dai, System-level performance optimization of molten-salt packed-bed thermal energy storage for concentrating solar power, Appl. Energy. 226 (2018) 225–239, https://doi.org/10.1016/j.apenergy.2018.05.081.

[39] B.C. Zhao, M.S. Cheng, C. Liu, Z.M. Dai, Thermal performance and cost analysis of a multi-layered solid-PCM thermocline thermal energy storage for CSP tower plants, Appl. Energy. 178 (2016) 784–799, https://doi.org/10.1016/j.apenergy.2016.06.034.

[40] P.A. Galione, C.D. Pérez-Segarra, I. Rodríguez, A. Oliva, J. Rigola, Multi-layered solid-PCM thermocline thermal storage concept for CSP plants. Numerical analysis and perspectives, Appl. Energy 142 (Mar. 2015) 337–351, https://doi.org/10.1016/j.apenergy.2014.12.084.

[41] S. Els, C.Xu ELSihy, X. Du, Numerical study on the dynamic performance of combined sensible-latent heat packed-bed thermocline tank, J. Energy Resour. Technol. Trans. ASME. 144 (1) (2022), https://doi.org/10.1115/1.4052466.

[42] S.C. Costa, M. Kenisarin, A review of metallic materials for latent heat thermal energy storage: thermophysical properties, applications, and challenges, Renew. Sustain. Energy. Rev. 154 (August) (2020) 2022, https://doi.org/10.1016/j.rser.2021.111812.

[43] C. Zhou, S. Wu, Medium- and high-temperature latent heat thermal energy storage: material database, system review, and corrosivity assessment, John Wiley and Sons Ltd, 2019.

[44] B. Cárdenas, N. León, High temperature latent heat thermal energy storage: Phase change materials, design considerations and performance enhancement techniques, Elsevier Ltd, 2013.

[45] B. Zalba, J.M. Marín, L.F. Cabeza, H. Mehling, Review on thermal energy storage with phase change: materials, heat transfer analysis and applications, Appl. Therm. Eng. 23 (3) (2003) 251–283, https://doi.org/10.1016/S1359-4311(02)00192-8.

[46] S.N. Gunasekara, V. Martin, J.N. Chiu, Phase equilibrium in the design of phase change materials for thermal energy storage: State-of-the-art, Elsevier. Ltd. (2017), https://doi.org/10.1016/j.rser.2017.01.108.

[47] C. E. Birchenall, S. I. Guyeri, D. Farkas, M. B. Labdon, N. Nagaswami, and B. Pregger, Heat Storage in Alloy Transformations, Mar. 1981.

[48] N. Sheng, et al., Development of a microencapsulated Al-Si phase change material with high-temperature thermal stability and durability over 3000 cycles, J. Mater. Chem. A. Mater 6 (37) (2018) 18143–18153, https://doi.org/10.1039/c8ta04708a.

[49] Vitaly Sobolev, Database of thermophysical properties of liquid metal coolants for GEN-IV, Boeretang, Belgium, 2011. [Online]. Available: http://www.sckcen.be.

[50] P.L. Kirillov, Thermophysical Properties of Materials for Nuclear Engineering : A Tutorial and Collection of Data, International Atomic Energy Agency, Vienna, Nov. 2008.

[51] H. Koide, et al., Performance analysis of packed bed latent heat storage system for high-temperature thermal energy storage using pellets composed of micro-encapsulated phase change material, Energy 238 (Jan. 2022), https://doi.org/10.1016/j.energy.2021.121746.

[52] E. Withey, A. Kruizenga, C. Andraka, P. Gibbs, Plasma sprayed coatings for containment of Cu-Mg-Si metallic phase change material, Surf. Coat. Technol 304 (Oct. 2016) 117–124, https://doi.org/10.1016/j.surfcoat.2016.06.063.

[53] V. Stahl, et al., C/C-SiC component for metallic phase change materials, Int. J. Appl. Ceram. Technol 17 (5) (Sep. 2020) 2040–2050, https://doi.org/10.1111/ijac.13570.

[54] J.L. Courouau, et al., Single crystal and sintered alumina corrosion in liquid sodium, Oxid. Met. 87 (5–6) (Jun. 2017) 789–800, https://doi.org/10.1007/s11085-017-9743-3.

[55] S. Khalid, A. Zakaria, W.A. Najmi, W. Mohamed, W. Azmi, W. Hamzah, Comparative analysis of thermophysical properties of Al 2 O 3 and SiO 2 nanofluids, J. Mech. Eng. 8 (1) (2019) 153–163.

[56] N. Boerema, G. Morrison, R. Taylor, G. Rosengarten, Liquid sodium versus Hitec as a heat transfer fluid in solar thermal central receiver systems, Sol. Energy 86 (9) (Sep. 2012) 2293–2305, https://doi.org/10.1016/j.solener.2012.05.001.

[57] J. Pietruszkiewicz et al., Solar Thermocline Storage Systems: Preliminary Design Study, Palo Alto, California (United States), 2010. doi: 10.2172/1488508.

[58] Accuratus, "99.5% Aluminum Oxide, Al2O3 Ceramic Properties." Accessed: Nov. 04, 2024. [Online]. Available: https://accuratus.com/alumox.html.

[59] A. Alemam, N. Lopez Ferber, T. Malm, V. Eveloy, N. Calvet, Experimental demonstration of a solar powered high temperature latent heat storage prototype, SolarPACES Conference Proceedings 2 (2024), https://doi.org/10.52825/solarpaces.v2i.968.

[60] A. Dindi, N. Lopez Ferber, D. Gloss, E. Rilby, N. Calvet, Compatibility of an Aluminium-Silicon metal alloy-based phase change material with coated stainless-steel containers, J. Energy. Storage 32 (September) (2020) 1–18, https://doi.org/10.1016/j.est.2020.101961.

[61] J.E. Rea, et al., Performance modeling and techno-economic analysis of a modular concentrated solar power tower with latent heat storage (Supplementary information), Appl. Energy 217 (February) (2018) 143–152, https://doi.org/10.1016/j.apenergy.2018.02.067.

[62] C.E. Andraka, A.M. Kruizenga, B. A. Hernandez-Sanchez, and E. N. Coker. Metallic phase change material thermal storage for dish Stirling, in: International Conference on Concentrating Solar Power and Chemical Energy Systems, SolarPACES, 2014, pp. 726–736. [Online]. Available: https://doi.org/10.1016/j.egypro.2015.03.083.

[63] M.M. Kenisarin, High-temperature phase change materials for thermal energy storage, Apr. 2010. doi: 10.1016/j.rser.2009.11.011.

[64] S. Höhlein, A. König-Haagen, D. Brüggemann, Macro-encapsulation of inorganic phase-change materials (PCM) in metal capsules, Materials 11 (9) (2018), https://doi.org/10.3390/ma11091752.

[65] A. Modi, C.D. Pérez-Segarra, Thermocline thermal storage systems for concentrated solar power plants: One-dimensional numerical model and comparative analysis, Sol. Energy 100 (2014) 84–93, https://doi.org/10.1016/j.solener.2013.11.033.

[66] K.A.R. Ismail, R. Stuginsky, A parametric study on possible fixed bed models for pcm and sensible heat storage, Appl. Therm. Eng 19 (7) (1999) 757–788.

[67] A. Elouali, et al., Physical models for packed bed: Sensible heat storage systems, J. Energy. Storage 23 (Jun. 2019) 69–78, https://doi.org/10.1016/j.est.2019.03.004.

[68] I. Calderón-Vásquez, et al., Review on modeling approaches for packed-bed thermal storage systems, Elsevier Ltd, 2021.

[69] A. de Gracia, L.F. Cabeza, Numerical simulation of a PCM packed bed system: A review, Elsevier Ltd, 2017.

[70] X. He, J. Qiu, W. Wang, Y. Hou, M. Ayyub, Y. Shuai, A review on numerical simulation, optimization design and applications of packed-bed latent thermal energy storage system with spherical capsules, Elsevier Ltd, 2022.

[71] S. Trevisan, Y. Jemmal, R. Guedez, B. Laumert, Packed bed thermal energy storage: A novel design methodology including quasi-dynamic boundary conditions and techno-economic optimization, J. Energy. Storage 36 (Apr. 2021), https://doi.org/10.1016/j.est.2021.102441.

[72] J. Beek, Design of packed catalytic reactors, Adv. Chem. Eng. 3 (1962) 203–271, https://doi.org/10.1016/S0065-2377(08)60060-5.

[73] J.F. Hoffmann, T. Fasquelle, V. Goetz, X. Py, A thermocline thermal energy storage system with filler materials for concentrated solar power plants: Experimental data and numerical model sensitivity to different experimental tank scales, Appl. Therm. Eng 100 (May 2016) 753–761, https://doi.org/10.1016/j.applthermaleng.2016.01.110.

[74] M. Cui, C. Zhang, B. Zhang, B. Xu, H. Peng, X. Wei Gao, Numerical solution of phase change heat transfer problems by effective heat capacity model and element differential method, J. Comput. Sci 60 (2022), https://doi.org/10.1016/j.jocs.2022.101593.

[75] N. Soares, P. Antunes, J.J. Costa, Effective heat capacity method to simulate heat difusion problems with phase change. in Energy for Sustainability International Conference, 2017.

[76] D. Pérez-Gallego, J. Gonzalez-Ayala, A. Medina, A. Calvo Hernández, Comprehensive review of dynamical simulation models of packed-bed systems for thermal energy storage applications in renewable power production, Elsevier Ltd, 2025.

[77] D. Poirier, M. Salcudean, On numerical methods used in mathematical modeling of phase change in liquid metals, J. Heat. Transfer 110 (3) (Aug. 1988) 562–570, https://doi.org/10.1115/1.3250529.

[78] E. Alptekin, M.A. Ezan, Performance investigations on a sensible heat thermal energy storage tank with a solar collector under variable climatic conditions, Appl. Therm. Eng 164 (Jan. 2020), https://doi.org/10.1016/j.applthermaleng.2019.114423.

[79] K.A.R. Ismail, J.R. Henriquez, Numerical and experimental study of spherical capsules packed bed latent heat storage system, Appl. Therm. Eng. 22 (15) (2002) 1705–1716.

[80] T. Esence, A. Bruch, J. F. Fourmigué, and B. Stutz, Extended modeling of packed-bed sensible heat storage systems, in: AIP Conference Proceedings, American Institute of Physics Inc., Nov. 2018. doi: 10.1063/1.5067101.

[81] E. Oró, J. Chiu, V. Martin, L.F. Cabeza, Comparative study of different numerical models of packed bed thermal energy storage systems, Appl. Therm. Eng. (2013) 384–392, https://doi.org/10.1016/j.applthermaleng.2012.07.020.

[82] Frank P. Incropera, David P. DeWitt, Theodore L. Bergman, Adrienne S. Lavine, Fundamentals of Heat and Mass Transfer, Sixth., vol. 85. J. Wiley & Sons, 2007. doi: 10.1016/S0263-8762(07)73214-8.

[83] N. Wakao, S. Kaguei, T. Funazkri, Effect of fluid dispersion coefficients on particle-to-fluid heat transfer coefficients in packed beds, Chem. Eng. Sci 34 (3) (1979) 325–336.

[84] J. Beek, Design of Packed Catalytic Reactors, in: Advances in Chemical Engineering, vol. 3, T. B. Drew, J. W. Hoopes, and T. Vermeulen, Eds., Academic Press, 1962, pp. 203–271. doi: https://doi.org/10.1016/S0065-2377(08)60060-5.

[85] J. Weiss, T.A. Bhanderi, T. Fluri, Impact of filler size and shape on performance of thermal energy storage, J. Energy. Storage 98 (Sep. 2024) 113157, https://doi.org/10.1016/j.est.2024.113157.

[86] A. Felix Regin, S.C. Solanki, J.S. Saini, An analysis of a packed bed latent heat thermal energy storage system using PCM capsules: Numerical investigation, Renew. Energy 34 (7) (2009) 1765–1773, https://doi.org/10.1016/j.renene.2008.12.012.

[87] S. Trevisan, R. Guedez, Design optimization of an innovative layered radial-flow high-temperature packed bed thermal energy storage, J. Energy. Storage 83 (Apr. 2024), https://doi.org/10.1016/j.est.2024.110767.

[88] E. A. Schmidt, M. Zehnder, F. Fellmoser, and K. Niedermeier, "UKHTC2024-007 Low-Prandtl Number Heat Transfer Fluids In Packed-Bed Heat Storage," 2024.

[89] B. Melissari, S.A. Argyropoulos, Development of a heat transfer dimensionless correlation for spheres immersed in a wide range of Prandtl number fluids, Int. J. Heat. Mass. Transf 48 (21–22) (Oct. 2005) 4333–4341, https://doi.org/10.1016/j.ijheatmasstransfer.2005.05.025.

[90] N. Nallusamy, S. Sampath, R. Velraj, Experimental investigation on a combined sensible and latent heat storage system integrated with constant/varying (solar) heat sources, Renew. Energy 32 (7) (Jun. 2007) 1206–1227, https://doi.org/10.1016/j.renene.2006.04.015.

[91] U.S. Energy Information Administration, "Electric Power Monthly with data for February 2025," 2025.

[92] M.I. Khan, et al., The economics of concentrating solar power (CSP): Assessing cost competitiveness and deployment potential, Elsevier. Ltd (2024), https://doi.org/10.1016/j.rser.2024.114551.

[93] L.F. Cabeza, M. Ibáñez, C. Solé, J. Roca, M. Nogués, Experimentation with a water tank including a PCM module, Sol. Energy. Mater. Sol. Cells 90 (9) (May 2006) 1273–1282, https://doi.org/10.1016/j.solmat.2005.08.002.

[94] C. Zauner, F. Hengstberger, B. Mörzinger, R. Hofmann, H. Walter, Experimental characterization and simulation of a hybrid sensible-latent heat storage, Appl. Energy 189 (2017) 506–519, https://doi.org/10.1016/j.apenergy.2016.12.079.

[95] L. Kasper, D. Pernsteiner, A. Schirrer, S. Jakubek, R. Hofmann, Experimental characterization, parameter identification and numerical sensitivity analysis of a novel hybrid sensible/latent thermal energy storage prototype for industrial retrofit applications, Appl. Energy 344 (Aug. 2023), https://doi.org/10.1016/j.apenergy.2023.121300.

[96] J.Y. Ryu, et al., A novel liquid air energy storage system using a combination of sensible and latent heat storage, Appl. Therm. Eng 203 (Feb. 2022), https://doi.org/10.1016/j.applthermaleng.2021.117890.